Chemical Geology 650 (2024) 121915

Contents lists available at ScienceDirect

Chemical Geology

journal homepage: www.elsevier.com/locate/chemgeo

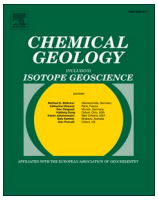

Reimagining Niggli Numbers for modern data applications in petrology and exploration geochemistry

Iain McDonald

School of Earth & Environmental Sciences, Cardiff University, Main College, Park Place, CF10 3AT, UK

ARTICLE INFO

Editor: Dr. Marco Fiorentini

Keywords:
Molecular Numbers
Constant Sum Problem
Bushveld Complex
Contamination
Hydrothermal Alteration
Chemostratigraphy

ABSTRACT

This study seeks to refamiliarize the geochemical community with Niggli Numbers and explore how Paul Niggli's largely forgotten scheme for representing major elements as equivalent molecular numbers that are combined as groups, sums and ratios. This scheme provides simple and effective tools for tackling many modern geochemical problems – particularly to reduce complexity and degrees of freedom where there are requirements to handle large volumes of data. Niggli Numbers provide an alternative to ratio-based methods for the long-recognised problem of the constant sum and data closure in geochemistry and offer a means to represent minerals and their relationships in a straightforward and consistent chemical framework. The Niggli calculation scheme follows simple rules that are easily automated, is flexible enough to accommodate missing elements or partial analyses, and is appropriate for all rock types. Following a short review of the most useful Niggli binary diagrams and where common minerals plot in Niggli space, a series of case studies are presented to illustrate potential applications of the scheme in modern petrology and resource exploration. These cover the following: magmatic evolution of a layered intrusion such as the Bushveld Complex; contamination of magmas by country rocks; tracing hydrothermal alteration in volcanogenic massive sulfide and porphyry Cu—Mo deposits; and chemostratigraphy of sedimentary sequences.

1. Introduction

Niggli Numbers are geochemical tools based on molecular values calculated from the percentage concentrations of oxides of the ten conventional major elements (Si, Ti, Al, Fe, Mn, Mg, Ca, Na, K and P) that are present in most common rocks and minerals. The calculation can also incorporate important trace elements like Cr, V, Ni, Ba, Sr, Rb, Cs and Li to augment the major elements, if these are available (Niggli, 1954). The calculation method and principles behind it were introduced by Paul Niggli in 1920 as classification tool and as a simplification of the earlier chemical classification of rocks developed by Osann (Niggli, 1920; Johannsen, 1931). While it is tempting to envisage rock chemistry as a 10 dimensional space between the major oxides, these components are not truly independent but instead interact through specific combinations that reflect the most common minerals. As will be shown below, Niggli Numbers provide a framework in which to both simplify this complexity and relate major element chemistry to mineralogy in a clear and effective manner.

Niggli Numbers are based on the concept of equivalent molecular numbers of component rock oxides (defined as the ratio of the weight percentage of an oxide component to its molecular weight). Importantly, the Niggli method avoids using SiO_2 as a factor in the primary number calculation step. This is deliberate and was designed as a means of avoiding bias associated with the closed sum problem and the concept of closure that is often most strongly influenced by SiO_2 as the dominant component in the majority of rocks (e.g. Chayes, 1960; Butler, 1981; Rollinson 1993; Buccianti and Grunsky, 2014). The mathematical problems associated with closure are significant and have led to the development of ratio-based approaches; including log-ratios (Aitchison, 1982), Pearce Element Ratios (PER; Pearce, 1968; Nicholls and Gordon, 1994) and General Element Ratios (GER; Stanley, 2020) as potential solutions. Niggli Numbers provide a simpler alternative to the closure problem because the calculation is critically reliant on only a portion of the major element composition and can readily accommodate missing elements or partial analyses where the resulting total is far from 100%. Indeed, an unexpected result arising from the mathematical analysis by Chayes (1968) found that correlations between Niggli Numbers were identical (within the limits of approximation) to those between the "remaining space transformation" variables that Chayes had developed to address the closed sum problem.

E-mail address: mcdonaldi1@cardiff.ac.uk.

https://doi.org/10.1016/j.chemgeo.2023.121915
Received 26 August 2023; Received in revised form 18 December 2023; Accepted 26 December 2023
Available online 30 December 2023

In the classic Niggli calculation, the molecular numbers associated with Al (plus Cr + V), Na + K (plus Cs + Li + Rb), Ca (plus Ba+Sr), and Fe + Mn + Mg (plus V + Ni) are combined in a sum and then expressed as percentages to create 4 primary Niggli Number values (designated *al*, *alk*, *c* and *fm* respectively) that always sum to 100. The molecular numbers for Si, Ti and P are then used to calculate 3 secondary numbers (designated *si*, *ti* and *p* respectively) that are scaled from the result of the sum of the primary molecular numbers, and in principle are free to range between zero and infinity. Individual Niggli Numbers can also generate useful ratios such as *al/alk*, *mg* (defined as the molecular number for MgO*/fm*) or *k* (defined as the molecular number for K_2O*/alk)* and also sums such as (*al-alk*) or ((*al* + *fm*)-(*c* + *alk*)). Silica saturation can also be expressed using sum terms designated *qz* (equal to *si*-(100 + 4*alk*) for rocks with *al/alk* > 1) or *qz** (equal to *si*-(100 + 3*al* + *1alk*) for rocks with *al/alk* < 1). Strongly negative values for *qz* or *qz** indicate that the rock is undersaturated and the mineralogy is dominated by silica deficient minerals such as feldspathoids, olivine, oxides, carbonates, etc. Positive values indicate silica oversaturation where mica, feldspars or clays are present and for strongly positive values (>200), the rock likely contains increasing amounts of free quartz. Niggli Numbers, ratios or sums can be plotted in relation to an independent parameter (e.g. distance or stratigraphic height), or in combination on binary or ternary diagrams.

The rules for the Niggli Number calculation are fully outlined in English in the review article by Muthuswami (1952) and the textbook by Niggli (1954). A spreadsheet to calculate Niggli Numbers is provided in Appendix A with two calculation schemes. "Niggli Classic" is the original scheme outlined in Niggli (1954) where Cr is combined as a trivalent ion with Al in the calculation for *al*. In mafic and ultramafic rocks that are rich in chromite, this artefact can make some data appear to fall in fields more typical of sediments rather than igneous rocks when plots involving *al* or the sum (*al-alk)* are used. "Niggli Modified" is a scheme that attempts to avoid this issue by combining Cr with Mg, Fe, Mn and Ni in the *fm* term, reflecting the natural association between Cr and Fe in many spinels and incorporation of significant Cr into important ferromagnesian minerals such as pyroxenes. The "Niggli Modified" scheme is preferred and has been adopted throughout this paper, but the classic scheme is provided for comparison and completeness.

As befits its development before digital computing, the Niggli Number calculation is designed to be simple and involve relatively few steps and assumptions. Measurement of silica, while desirable, is not essential and data obtained from analysis schemes that employ hydrofluoric acid and consequently lose Si during evaporation (an analysis process widely used in exploration geochemistry) will still produce meaningful values for all Niggli Numbers other than *si* (and its derivatives *qz* and *qz**). The process of combining multiple elements into single terms like *alk* or *fm* and scaling based on the result of the primary molecular sum are not only simplifications intended to ease calculation. The Niggli scheme offers inherent design advantages that reduce scatter during data plotting, simplify the number of degrees of freedom needed to represent minerals, and help circumvent the mathematical challenges imposed by closure. Niggli Numbers can be calculated for any rock or mineral as long as data for some or all the elements required for the 4 primary numbers are available. Furthermore, the simplifications also obviate the need to measure (or assume): the oxidation state of iron (as Fe^{2+} and Fe^{3+} are combined in a single term); the volatile content of the rock; or determine the exact nature of any volatiles. These are all factors which can critically affect calculation of Mg# values or normative mineralogy. If volatile data are available, additional secondary Niggli Numbers for *CO_2, SO_2, Cl_2, F_2, S and H_2O* can be determined (Niggli, 1954) and are also included in Appendix 1 – although these are less commonly used. Compared to common normative mineral schemes (e.g. CIPW norms; Cross et al., 1903), Niggli numbers follow simpler rules with fewer pre-requisites and underlying assumptions, are robust enough to accommodate missing elements or changes in data formatting (e.g. FeO, Fe_2O_3, $FeO_{(total)}$ or $Fe_2O_{3(total)}$) between different datasets, and are relevant for any common mineral or rock type: whether it is igneous, metamorphic or sedimentary; and whether it is volatile-rich or volatile-poor.

Primary and secondary Niggli Numbers do not involve the additional step of expressing each molecular number as a ratio with another element that is either assumed to be conserved during mass transfer, as in the case of Pearce Element Ratios (Pearce 1968), or unconserved during mass transfer, as in the case of General Element Ratios (Stanley, 2017, 2020). Instead the molecular numbers are always expressed as percentages relative to the value of the primary number sum. This inherently limits variation between the 4 primary numbers, while allowing the secondary *si, ti* and *p* numbers greater potential dynamic range. The deliberate use of sums like (*al-alk*) also distinguishes Niggli Numbers from ratio-based analysis schemes. While they only involve major elements (plus a few trace elements), Niggli Numbers are complementary with many of the applications of GER analysis in lithogeochemistry highlighted by Stanley (2020). As will be illustrated below, by careful selection of numbers or sums on different plot axes, it is possible to define nodes or trends where a mineral or rock type must exist, and where its influence on a suite of samples can be inferred.

Niggli Numbers were originally designed for broad rock classification by visualising the *al*, *fm*, *alk* and *c* terms as the points of a concentration tetrahedron (Niggli, 1954). This could be further extended to a double tetrahedron by incorporating positive and negative results for (*al-alk*) and triangular plots created using sections through the tetrahedron could be used to create fields for classifying different types of rock within *al-fm-alk-c* space (Niggli, 1954). This expanded further into studies of igneous petrogenesis and magma evolution (Niggli, 1952; Coats, 1952) and subsequently into provenance determination and deriving original petrogenetic associations in high-grade metamorphic rocks of ambiguous origin (e.g. Evans and Leake, 1960; Leake and Skirrow, 1960).

It is important to remember that Niggli's scheme was introduced and reached its widest use at a time before the x-ray fluorescence spectrometer not only replaced laborious wet chemical and gravimetric analysis for major elements but also provided a means to determine a useful suite of trace elements at the same time. Because they rely primarily on major elements, Niggli Numbers were unfairly perceived as being limited in scope when abundant trace element data also became available. Studies using Niggli Numbers become rarer from the 1970's onward as they were supplanted by other major element classification schemes such as TAS (Total Alkali-Silica; Le Maitre et al., 1989) or those based primarily on trace elements or isotopes, and appeared in the literature only when championed by a small community who continued to see their utility and value (e.g. Senior and Leake, 1978; Rehkopff, 1984; Leake and Singh, 1986; van de Kamp and Leake 1995; Abdel-Karim et al., 2002; Zheng et al., 2013). Indeed it is striking that all of the studies cited above that highlighted valid concerns around closure and the constant sum problem post-date the development of Niggli Numbers, yet only Chayes (1968) mentions them briefly as an alternative potential solution. It would not be unfair to state that today Niggli Numbers have sadly been reduced to little more than a historical footnote - unknown to the vast majority of geochemists and mentioned only in passing (if at all) in the last 50 years-worth of textbooks devoted to training students in petrology and geochemistry.

Even in the method's heyday, major constraints were that only limited volumes of data were available for any suite of rocks, and Niggli Number calculations and data plotting were necessarily performed by hand. Burri and Niggli (1945, 1949) calculated and collated Niggli Numbers based on available analyses for suites of rocks throughout Europe, the Americas and Africa but even this comprehensive work contains less than a few thousand analyses and sets of numbers, and with only limited discussion of the likely mineralogical controls. The simplicity of Niggli Numbers and the ways in which they can be combined to represent mineralogy are ideally suited to the modern world of big data applications where effective and efficient tools are desired to

reduce complexity and maximise time and value (He et al., 2022). The aim of this paper is to refamiliarize the geochemistry community with Niggli Numbers and demonstrate both their ease of use and applicability to topics beyond those they were originally designed to address. These are presented in Sections 2 and 3 as a series of example diagrams and application case studies that include: (i) magmatic evolution in layered intrusions; (ii) contamination and hybridization of magma with different country rocks and the associated implications for mineralization; (iii) characterization of different styles of alteration associated with hydrothermal mineralization in volcanogenic massive sulfide and porphyry copper deposits; and (iv) chemostratigraphy of sedimentary rocks and stratigraphic correlation in "difficult" sequences such as continental basins where the use of biostratigraphy may be challenging or impossible.

2. Minerals, rocks and processes represented by some Niggli Number plots

As the primary Niggli Numbers (*al, alk, c* and *fm*) must sum to 100, scales involving primary numbers alone range from 0 to 100 while their sums can potentially range from −100 to +100. As will be shown below, if sums (e.g. *al-alk*) are chosen to reflect a natural substitution in particular minerals then whether a net result is positive, zero or negative (and its magnitude) may directly track an aspect of the rock mineralogy. Scales for the secondary numbers *si, ti* and *p* are not constrained in this way and pure end member forms of SiO_2 and TiO_2 that contain none of the primary Niggli elements, in principle produce *si* and *ti* values of infinity. However, as natural quartz and rutile always contain some trace elements that contribute to the primary Niggli Numbers, these infinities do not arise in the real world. The following sections will illustrate how different numbers or sums can be used on a variety of useful binary plots. These plots display fields for different minerals in Niggli space. Minerals can be identified by a consistent abbreviation and colour in each of these diagrams (see Fig. 1 for a full explanation). The relevant data sources for rocks and minerals (and whether any primary source data have been reduced by filtering) for all of the plots presented in subsequent sections are provided in Table 1.

2.1. *(al-alk) versus c*

One of the oldest and most well-known Niggli plots is (*al-alk)* versus *c* and fields for the natural compositions of various minerals are shown in Fig. 1. Minerals such as quartz or olivine that typically lack Al, Na, K or Ca plot at the origin. Calcium-free minerals with equal proportions of *al* and *alk* such as orthoclase, nepheline, leucite or albite (An_0) also plot on or close to the origin and a line (hereafter referred to as the plagioclase line) between albite and anorthite (An_{100}) represents the composition of any plagioclase feldspar in (*al-alk)* versus *c* space. The majority of silicates, carbonates and oxides have (*al-alk)* values of zero or greater. Cordierite and staurolite are not shown in Fig. 1 for reasons of space but are restricted to the y-axis at (*al-alk*) values close to 50 and 75 respectively. Na-rich silicates such as riebeckite and aegirine plot at negative (*al-alk*) and mineral forms of pure alkali chlorides such as halite or sylvite would plot at (*al-alk*) values of −100.

The field for typical igneous rocks originally defined by Niggli et al. (1930) is shown by the red dashed field in Fig. 1. This field is constrained by possible combinations of the most common igneous minerals, with the open space around it either reflecting possible alteration/contamination (see below) or forbidden space where no thermodynamically stable minerals exist. Mafic igneous rocks such as peridotites, norites, troctolites and anorthosites fall on or close to the plagioclase line. Rocks containing clinopyroxene or amphibole will plot progressively to the right of and below the line as the proportions of these minerals increase. Igneous rocks with biotite or muscovite may plot to the left of the plagioclase line depending on the mica content. Differentiation will cause evolving suites of rocks to move towards and descend the

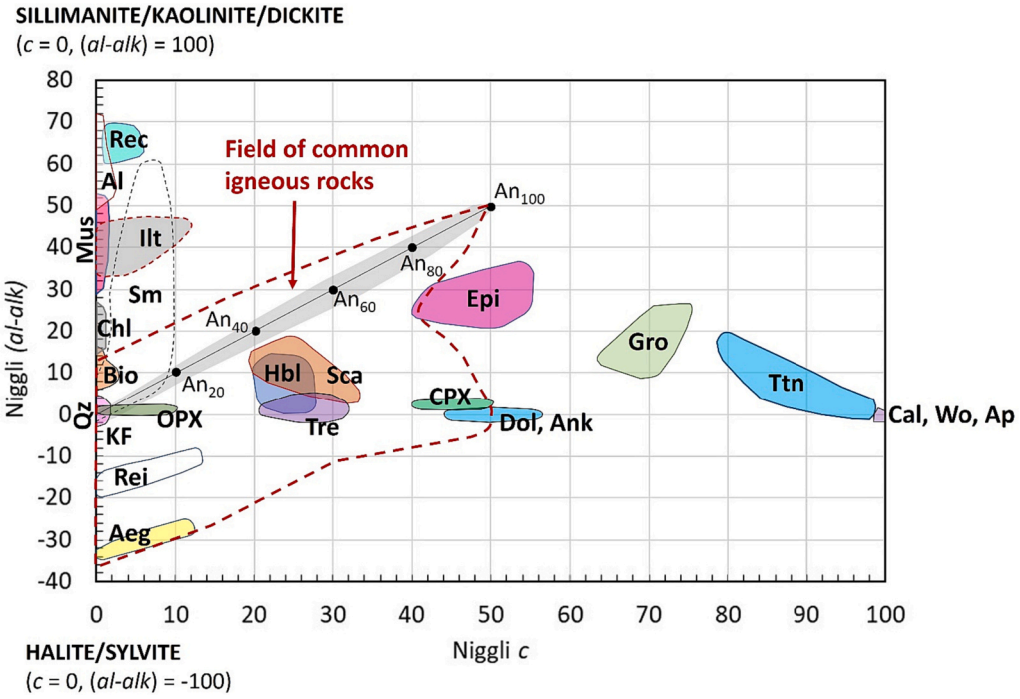

Fig. 1. Niggli (*al-alk*) versus *c* diagram with fields for common minerals as follows; Cal (calcite), Wo (wollastonite), Ap (apatite), Ttn (titanite), Gro (grossular), Dol (dolomite), Ank (Ankerite), CPX (Augite and Diopside), Epi (epidote), Sca (scapolite), Hbl (hornblende), Tre (tremolite-actinolite), Aeg (aegirine), Rei (riebeckite), KF (K feldspar), Qz (quartz), OPX (orthopyroxene and pigeonite), Bio (biotite), Chl (chlorite), Mus (muscovite), Sm (smectite-montmorillonite), Ilt (illite), Al (alunite) and Rec (rectorite). The field of typical igneous rocks defined by Niggli et al. (1930) is shown by a red dashed line. Data used to create the mineral fields are listed in Table 1. Kaolinite, sillimanite, dickite, halite and sylvite plot outside the scale shown in the Figure, as indicated in the text. (For interpretation of the references to colour in this figure legend, the reader is referred to the web version of this article.)

Table 1
Compilation of data sources for Niggli Number calculations and plots

Mineral Data	N	Data source(s)	Filtered (Y/N)
Biotite	3713	DIGIS Team, 2023k; Panigrahi et al., 2008; Afshooni et al., 2013; Parsapoor et al., 2015	Y (Biotite)
Muscovite	248	DIGIS eam, 2023k; Parry et al., 1984; Kim et al., 1992; Runyon et al., 2019	Y (Muscovite)
Alunite	15	Mavrogonatos et al., 2018	N
Scapolite	16	David Holwell (pers comm)	N
Illite-smectite	176	DIGIS Team, 2023g; Środoń et al., 1986	Y (Illite and Smectite)
Stilpnomelane	10	Miyano and Beukes, 1984	N
Reibeckite	47	DIGIS Team, 2023e; Miyano and Beukes, 1984	Y (Reibeckite)
Albite	1385	DIGIS Team, 2023i; Barros et al., 2020	Y (Albite)
Aegerine	5	Miyano and Beukes, 1984	N
Chlorite	479	Panigrahi et al., 2008; Afshooni et al., 2013; Xiao et al., 2018	N
Epidote	138	Xiao et al., 2018	N
Hornblende	3756	DIGIS Team, 2023e; Dessimoz et al., 2012	Y (Hornblende)
Titanite	548	DIGIS Team, 2023n; Gros et al., 2020	N
Grossular	35	DIGIS Team, 2023j; Antao, 2021	Y (Grossular)
Rectorite	4	Środoń et al., 1986	N
Actinolite	80	DIGIS Team, 2023e	Y (Actinolite)
Tremolite	93	DIGIS Team, 2023e	Y (Tremolite)
Montmorillonite	40	DIGIS Team, 2023g	Y (Montomorillonite)
Ankerite	192	DIGIS Team, 2023f	Y (Ankerite)
Dolomite	783	DIGIS Team, 2023f	Y (Dolomite)
Orthoclase	1013	DIGIS Team, 2023i	Y (Orthoclase)
Plagioclase	3857	DIGIS Team, 2023i; Ashwal et al., 2005; Roelofse and Ashwal, 2012;	Y (Plagioclase, Layered Intrusion)
Clinopyroxene	4277	DIGIS Team, 2023h; Ashwal et al., 2005; Roelofse and Ashwal, 2012	Y (Clinopyroxene, Layered Intrusion)
Low-Ca pyroxene	521	Ashwal et al., 2005; Roelofse and Ashwal, 2012; Hulbert, 1983	N
Chromite	616	DIGIS Team, 2023m	Y (Chromite, Bushveld Complex)
Olivine	861	DIGIS Team, 2023l	Y (Olivine, Bushveld Complex)
Whole Rock Data	**N**	**Data source(s)**	**Filtered (Y/N)**
Convergent Margin andesites	2276	DIGIS Team, 2023a	Y (Convergent margin, <1.5% LOI)
Convergent Margin basalts	736	DIGIS Team, 2023b	Y (Convergent margin, <1.5% LOI)
Convergent Margin dacites	992	DIGIS Team, 2023c	Y (Convergent margin, <1.5% LOI)
Convergent Margin rhyolites	315	DIGIS Team, 2023d	Y (Convergent margin, <1.5% LOI)
Intraplate carbonatites	1179	DIGIS Team, 2023o	N
Kimberlites	4722	DIGIS Team, 2023p	N
Nephelinites	338	DIGIS Team, 2023q	N
Continental Flood Basalt Province gabbro	1656	DIGIS Team, 2023r	Y (CFB provinces)
Du Bray Nevada dacite	34	Du Bray et al., 2007; du Bray et al., 2022	Y (Dacite, <1.5% LOI)
Du Bray Nevada dacite - argillic	15	Du Bray et al., 2007; du Bray et al., 2022	Y (Dacite, alteration argillic)
Du Bray Nevada dacite - phyllic	13	Du Bray et al., 2007; du Bray et al., 2022	Y (Dacite, alteration phyllic)
Du Bray Nevada dacite - propylitic	9	Du Bray et al., 2007; du Bray et al., 2022	Y (Dacite, alteration propylitic)
Du Bray Nevada granodiorite	197	Du Bray et al., 2007; du Bray et al., 2022	Y (Granodiorite, <1.5% LOI)
Du Bray Nevada granodiorite - phyllic	6	Du Bray et al., 2007; du Bray et al., 2022	Y (Granodiorite, alteration phyllic)
Du Bray Nevada granodiorite - potassic	15	Du Bray et al., 2007; du Bray et al., 2022	Y (Granodiorite, alteration potassic)
Du Bray Nevada granodiorite - propylitic	70	Du Bray et al., 2007; du Bray et al., 2022	Y (Granodiorite, alteration propylitic)
Hongtoushan volcanics	51	Zheng et al., 2013	N
Le Grande Sud complex	45	Mercier-Langevin (2000)	N
RLS Basal Ultramafic Series (E Limb)	622	Wilson, 2015	N
RLS Lower Zone (W Limb)	75	Teigler and Eales, 1996	N
RLS Lower Zone (N Limb)	121	Hulbert, 1983; Maier et al., 2008; McDonald et al., 2009; Yudovskaya et al., 2013; Smith, 2014	N
RLS Lower Critical Zone (W Limb)	53	Teigler and Eales, 1996	N
RLS Upper Critical Zone (W Limb)	51	Cawthorn et al. 1996; de Klerk, 1991	N
RLS Upper Critical Zone (E Limb)	520	Wilson and Chunnett, 2006; Seabrook, 2005	N
Platreef-Critical Zone (Grasvally-Rooipoort)	136	Hulbert, 1983; Maier et al., 2008; Smith, 2014	N
Platreef-Critical Zone (Townlands)	18	Manyeruke et al., 2005	N
Platreef-Critical Zone (Turfspruit)	110	Yudovskaya et al., 2013; Nodder, 2015; Keir-Sage et al., 2021	N
Platreef-Critical Zone (Tweefontein)	50	Ihlenfeld and Keays, 2011	N
Platreef-Critical Zone (Sandsloot)	81	Harris and Chaumba, 2001; McDonald et al., 2005; Holwell, 2006; Ihlenfeld and Keays, 2011	N
Platreef-Critical Zone (Overysel)	65	Holwell, 2006; Ihlenfeld and Keays, 2011	N
RLS Main Zone (E Limb)	110	Seabrook, 2005; Lundgaard et al., 2006; Setera and VanTongeren, 2018	N
RLS Main Zone (W Limb)	52	Nex et al., 2002; Mitchell and Manthree, 2002	N
RLS Lower Main Zone (N Limb)	198	van der Merwe, 1978; Roelofse and Ashwal, 2012; Kennedy, 2019	N
Troctolite Unit and Upper Main Zone (N Limb)	150	van der Merwe, 1978; Kennedy, 2019	N
RLS Upper Zone (W Limb)	260	Yuan et al., 2017	N
RLS Upper Zone (E Limb)	62	Vantongeren et al., 2010	N
RLS Upper Zone (N Limb)	15	van der Merwe, 1978; Hulbert, 1983	N
Waterberg F Zone-Troctolite-T Zone (N Limb)	128	McCreesh, 2016	N
Waterberg Upper Zone (N Limb)	47	McCreesh, 2016	N

(*continued on next page*)

Table 1 (*continued*)

Mineral Data	N	Data source(s)	Filtered (Y/N)
Malmani and Ramoneddi dolomite formations	55	Harris and Chaumba, 2001; McDonald et al., 2005; Franchi, 2018; Ihlenfeld and Keays, 2011	N
Penge ironstone formation	20	Miyano and Beukes, 1997; Ihlenfeld and Keays, 2011	N
Duitschland formation	30	Stephenson, 2019; Keir-Sage et al., 2021	N
Hout River gneiss and granite	26	Cawthorn et al., 1985; Holwell, 2006	N
Obernsees-1 sedimentary sequence	203	Ravidà et al. (2023)	N
Lindau-1 sedimentary sequence	150	Ravidà et al. (2023)	N

plagioclase line. This is illustrated for a large dataset in Fig. 2 using 4327 sets of Niggli Numbers calculated from relatively fresh whole rock analyses (filtered to <1.5% Loss on Ignition) for convergent margin basalts, andesites, dacites and rhyolites. Only a few data points fall outside the typical igneous field and moving from basalt to rhyolite, the expected progressive shifts towards lower *c* values and then down the plagioclase line towards albite and quartz are clearly evident (Fig. 2).

A simplified version of the (*al-alk*) versus *c* plot focused on common minerals in sedimentary rocks is shown in Fig. 3a. Burri and Niggli (1945) and Niggli (1954) observed that clastic and mixed clastic-carbonate sedimentary rocks tend to occupy fields that slope steeply from the clay field at the top left towards quartz and K feldspar at the origin, or negatively from left to right towards dolomite or calcite (Fig. 3a). These sedimentary fields are distinctive and, in the case of carbonate-rich sediments, trend at right angles to the plagioclase line and the normal differentiation trend for igneous rocks. Where igneous intrusions assimilate and metamorphose carbonate-rich sedimentary country rocks, an additional field shown in Fig. 3b can be drawn to cover magnetite-olivine-orthopyroxene-tremolite-actinolite-epidote-dolomite-ankerite-grossular-calcite-wollastonite. This combined field extends significantly to the right of the common igneous field and encompasses the majority of potential minerals found in Ca-Mg-Fe carbonate metamorphic aureoles and skarns.

2.2. *(al + fm)-(c + alk) versus si*

A Niggli plot using a sum involving all of the primary numbers combined with a variable that generally increases with differentiation is (*al* + *fm*)-(*c* + *alk*) versus *si* (Fig. 4). This is superficially similar to a conventional Harker diagram with SiO_2 on the x-axis, but with additional features. In this space, pure silica minerals lie at infinity on the *si* axis but fields for other common minerals are mostly restricted to *si* values between 0 and 300. Therefore, in most cases it can be assumed that any whole rock analysis producing *si* > 300 must contain free silica (typically quartz) mixed with other mineral components. The (*al* + *fm*)-(*c* + *alk*) term is an expansion of the (*al-alk*) term introduced previously that operates on a similar −100 to +100 scale, but allows for more minerals to be separated and distinguished. Carbonates, halides, oxides and Fe-bearing sulfides are restricted to the (*al* + *fm*)-(*c* + *alk*) axis. Olivine, chlorite and serpentine form a discrete field at (*al* + *fm*)-(*c* + *alk*) = 100 and *si* ~ 50 separated from the other silicates. All plagioclase has (*al* + *fm*)-(*c* + *alk*) near zero and extends from *si* = 100 (An_{100}) to *si* = 300 (An_0). Only a few common minerals such as scapolite, grossular, titanite, calcite, apatite, wollastonite and alkali halides fall below (*al* + *fm*)-(*c* + *alk*) = 0.

The main use of this diagram in previous studies has been to establish an igneous or sedimentary origin for ambiguous high grade gneisses or suspected intrusions. Zheng et al. (2021) defined a sediment field and one for "typical igneous rocks" shown in grey in Fig. 5a. This field encompasses nearly all of the convergent margin volcanic rocks discussed in Section 2.1 (Fig. 5a) but its utility breaks down when applied to alkaline igneous rocks, especially those containing major or minor carbonate component, or to plutonic suites such as the collisional margin granodiorites. Significant numbers of these are scattered outside, reflecting fractionation and accumulation of carbonates, olivine,

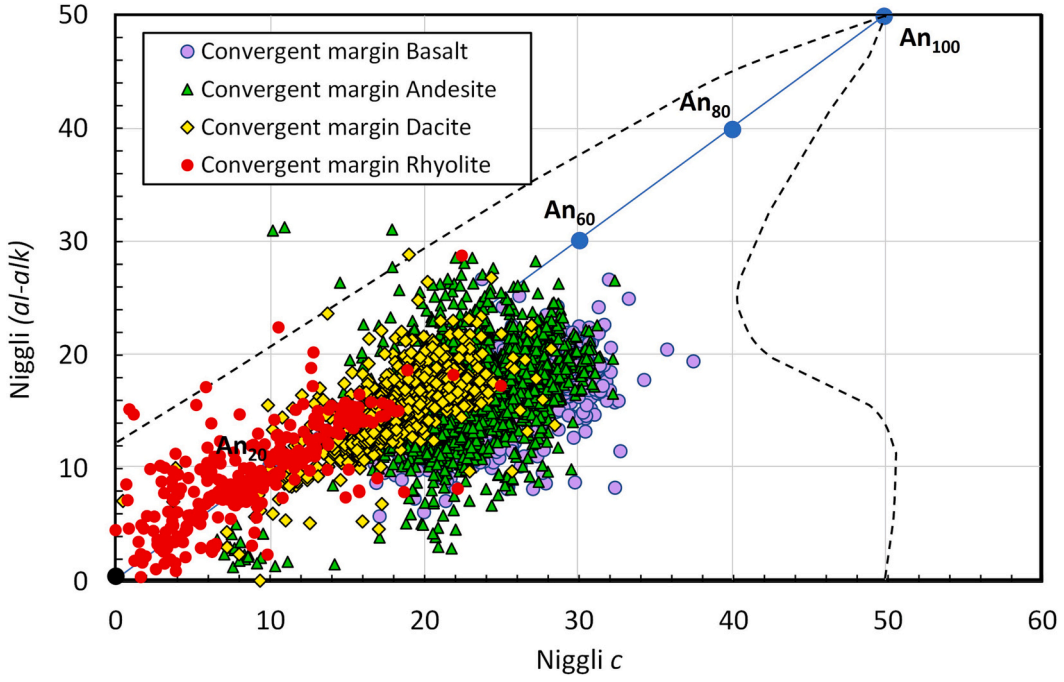

Fig. 2. Niggli (*al-alk*) versus *c* diagram with data shown for basalts, andesites, dacites and rhyolites from convergent margin settings, as listed in Table 1. Part of the field for typical igneous rocks is shown as a dashed black line.

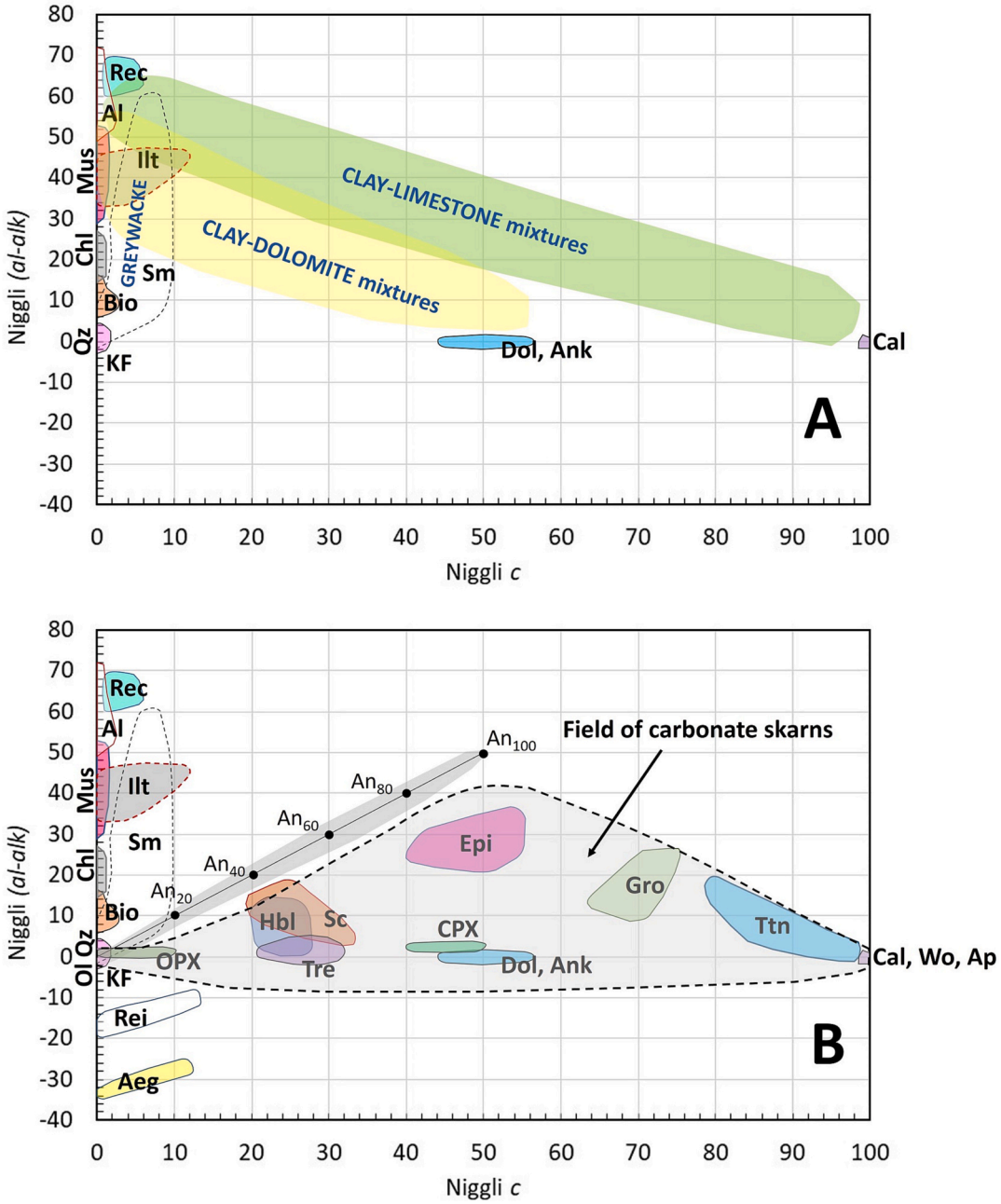

Fig. 3. (A) Niggli (*al-alk*) versus *c* diagram showing trends for carbonate-bearing sedimentary rocks involving mixtures of clay with dolomite or calcite based on Niggli (1954); (B) Niggli (*al-alk*) versus *c* diagram with a potential field for minerals present in carbonate/calc-silicate skarns.

pyroxenes or micas compared to the "typical" field (Fig. 5b). The utility of this plot however goes far beyond a simple igneous or non-igneous characterization and it allows potential mineral associations to be tested using appropriate data.

For example, Fig. 6a shows a $(al + fm)$-$(c + alk)$ versus *si* diagram that can be used to represent crystallization of cumulate rocks in layered mafic intrusions. On Niggli plots, minerals occupy fields that are centred on nodes where data density is highest. Simple tie lines can be accurately drawn between nodes to compare real data against a model co-crystallization of two phases, or tie lines can be linked into polygons to investigate crystallization or accumulation of three or more minerals. The compositions of spinels such as chromite or magnetite (V), olivine (W), Low-Ca pyroxene (X), clinopyroxene (Y), plagioclase (Z) are shown along with tie lines between different mineral pairs in Fig. 6a. Points X and Y are nodes with the highest density of pyroxene data within each respective field and the positions of these nodes are largely unchanged by the Fe/Mg ratio of the pyroxene. The *si* value of plagioclase will vary with its anorthite content and a nominal value An_{80} was chosen for point Z in the example in order to simulate the average plagioclase composition in the Upper Critical Zone (UCZ) of the eastern Bushveld Complex (Eales and Cawthorn, 1996). The same whole rock UCZ data taken from Seabrook (2005) are compared on the Niggli $(al + fm)$-$(c + alk)$ versus *si* diagram in Fig. 6a and a conventional Harker diagram plotting either MgO or CaO versus SiO_2 in Fig. 6b. The UCZ data are more tightly clustered along the orthopyroxene-plagioclase tie line XZ. Some deviations from XZ track towards W, reflecting the presence of olivine. However, there are points that lie to the left of the olivine-plagioclase tie line WZ and which fall on obvious vectors towards the spinel field at V, as highlighted by red arrows. These indicate samples with elevated levels of chromite. Such trends are not as easily visible on the Harker

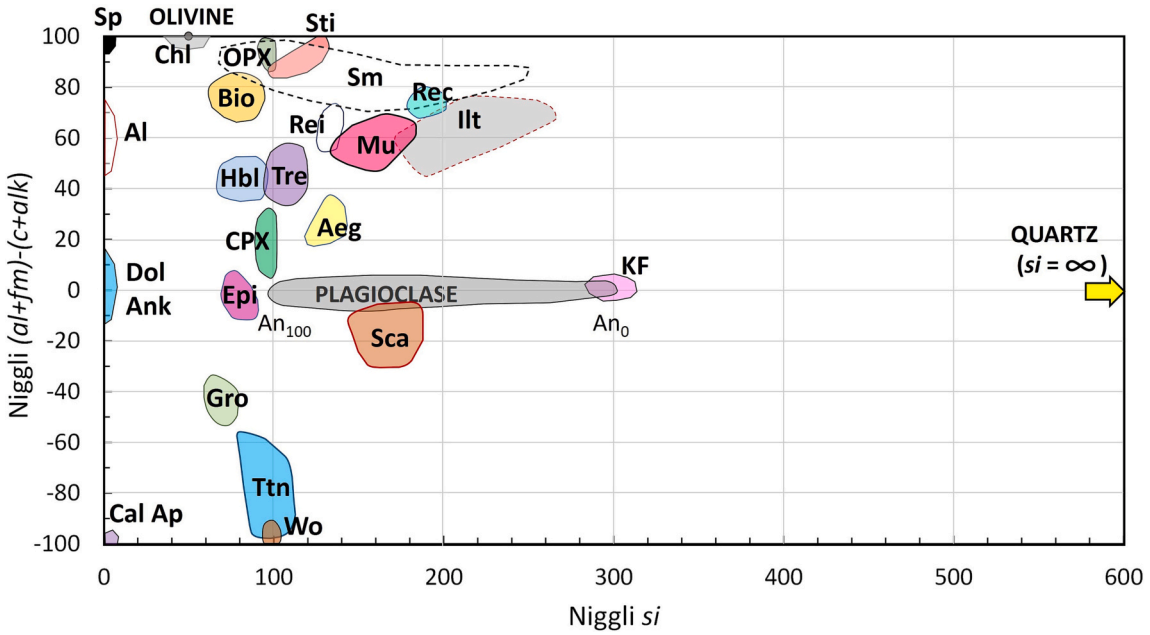

Fig. 4. Niggli (*al* + *fm*)-(*c* + *alk*) versus *si* diagram with fields for common minerals. Abbreviations as in Fig. 1. Data used to create the mineral fields are listed in Table 1.

plot, where data fall on more scattered trends between more poorly defined fields. This analysis is expanded in Section 3.1 where the magmatic evolution of a layered mafic intrusion such as the Bushveld Complex is addressed.

2.3. *(al-alk) versus (al + fm)-(c + alk)*

This diagram with two Niggli sums combines useful elements already outlined in Sections 2.1 and 2.2. Fields for common minerals are shown in Fig. 7. Quartz, K feldspar and albite plot at the origin and the field for plagioclase defines a vertical line. A simplified version focused on the top right hand quadrant where the majority of silicate minerals are found is shown in Fig. 8. The field for common non-alkaline igneous rocks is bounded by the box defined by OL (olivine), OPX (orthopyroxene), AN (anorthite) and QZ (quartz). Increasing fractionation, illustrated by the data for convergent margin volcanic rocks, follows a curved and negatively sloping trend towards quartz and alkali feldspar (Fig. 8a). Data for the layered pyroxenites, norite and anorthosites of the Eastern Bushveld UCZ compared with global data for gabbros from Continental Flood Basalt (CFB) provinces are summarised in Fig. 8b and highlight that the layered mafic cumulates fall on well-defined trends between olivine-orthopyroxene and plagioclase (approximately An_{80}) that reflect the relative proportions of feldspar and mafic silicates in the rock. In contrast the gabbro data occupy a wedge-shaped field defined by a narrower range of *al-alk* and (*al* + *fm*)-(*c* + *alk*) values that reflect greater average amounts of clinopyroxene. Fractionation, magma mixing or other strictly igneous processes operating in silicate magmas are highly unlikely to move the composition to the left of the quartz-plagioclase line or above the tie line between anorthite and orthopyroxene. With the exception of titanite (which can be assumed to be a minor accessory in the vast majority of cases), these areas are dominated by metamorphic or alteration minerals and nominally "igneous" rocks the plots on points lying outside the OL-OPX-AN-QZ polygon are highly likely to be altered or contaminated by sedimentary rocks. This will be explored in greater depth in Sections 3.2 and 3.3 that deal specifically with contamination and alteration.

2.4. *(al-alk) versus k*

In previous sections, Na and K have been considered together as the combined *alk* term but there are many situations where it is valuable to distinguish them and the (*al-alk*) versus *k* plot shown in Fig. 9 is a useful tool for this. Minerals that lack alkalis cannot be reliably plotted but many important alteration minerals can be distinguished. Albite and K Feldspar plot at (*al-alk*) = 0 and *k* values close to 0 and 1 respectively. Na-rich minerals such as riebeckite, aegirine and scapolite have *k* close to zero and distinctive (*al-alk*) values (Fig. 9a). Biotite, muscovite and stilpnomelane are similarly spread on the opposite side of the diagram. Illite, rectorite, smectite-montmorillonite, chlorite and alunite define broad fields across variable *k* values and are more readily separated from each other on this plot than on the (*al-alk*) versus *c* or the (*al-alk*) versus (*al* + *fm*)-(*c* + *alk*) diagrams previously described. Convergent margin volcanics define curving data clusters that trend towards higher *k* and lower (*al-alk*) with fractionation but even for rhyolites, *k* values >0.5 are uncommon. In contrast, silica-poor alkaline igneous rocks such as carbonatites, kimberlites and melilitites span the full range of *k* values at near to (*al-alk*) = 0 (Fig. 9b). Further applications of this diagram are explored in Section 3.3.

2.5. *ca versus mg*

This diagram was introduced by Leake (1964) to help define reliable geochemical criteria for distinguishing amphibolite facies metamorphic rocks formed from igneous versus sedimentary precursors. Fields for common minerals in *ca* versus *mg* space are shown in Fig. 10a. Olivine, low-Ca pyroxenes and biotite define a field spanning the full *mg* range at the bottom of the diagram. Chlorite also has low or zero *c* but occupies a narrower range of *mg* values. Natural magnesite often contains some Ca and forms a vertical field close to *mg* = *1* while data for epidote, grossular titanite and apatite define fields at different *c* values on or near the *mg* = 0 axis. Plagioclase and other common igneous minerals are restricted to the lower half of the diagram and this is expanded in Fig. 10b to show the best fit "igneous trend" through data from 80 Karoo dolerites, and the field for "pelites and semi-pelites" proposed by Leake (1964). Layered igneous cumulates formed from tholeiitic magmas containing different proportions of plagioclase and olivine/

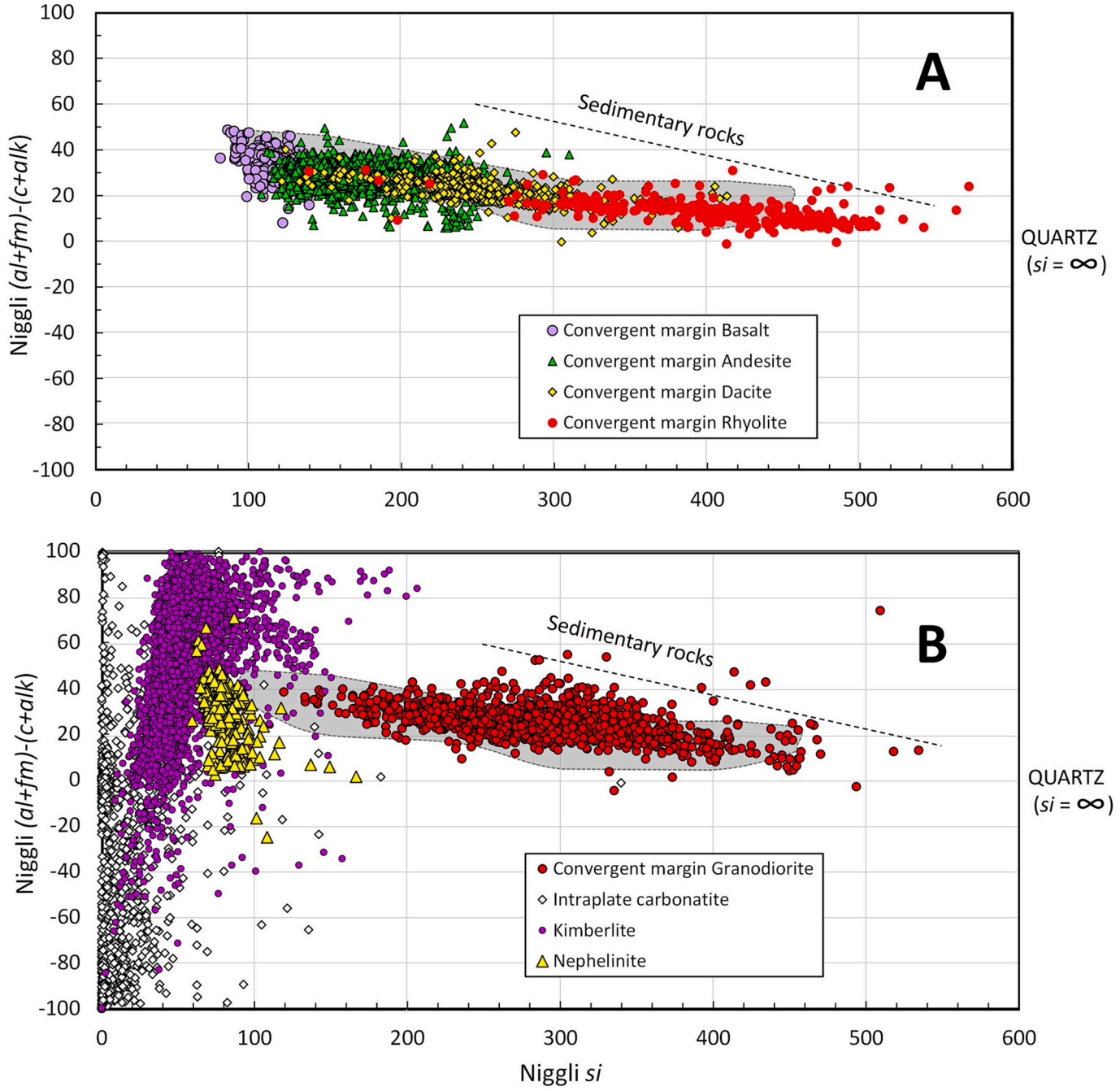

Fig. 5. Niggli (*al* + *fm*)-(*c* + *alk*) versus *si* diagrams. (A) data for basalts, andesites, dacites and rhyolites from convergent margins compared to the fields for sediments and "typical igneous rocks" from Zheng et al. (2021); (B) data for convergent margin granodiorites, nephelinites, kimberlites and intraplate carbonatites compared to the Zheng et al. (2021) fields. Data sources are listed in Table 1.

orthopyroxene should follow steep parabolic curves such as the model curve in red between An_{80} and En_{81} end members. This model effectively traces the trend of real data from the Eastern Bushveld UCZ (Seabrook, 2005) where co-crystallization of these two minerals, along with minor olivine and chromite, is the norm.

The large dataset for convergent margin volcanic rocks defines a wide field that partly follows the Leake (1964) igneous trend except below *mg* = 0.4, where most dacites and rhyolites lie significantly below the projected line (Fig. 10c). Whether magmas fractionate clinopyroxene or amphibole (or not) will strongly influence the height and curvature of any trend defined by whole rocks and, as shown above, this can be modelled if Niggli Numbers are also calculated for the compositions of the major mineral components at different stages of crystallization. Alkaline rocks containing significant carbonate such as kimberlite or carbonatite follow separate trends controlled by the relative proportions of silicate minerals and the dominant carbonate phase (Fig. 10c).

In sedimentary rocks, values for *c* will be buffered to a limited extent by the composition of any plagioclase but a greater influence will be exerted by the amount of any carbonate, whether primary or secondary, present in the rock. Data for Californian arkoses (Van De Kamp et al., 1976) and for Late Palaeozoic shales, siltstone and sandstones from Colorado (Cullers, 2000) are shown in Fig. 10d. The Colorado data with the lowest *c* values spread across a wider range of *mg* (0.1–0.55) than Leake's original pelite field and the other data define near-vertical trends between these and calcite, or positively sloping trends towards dolomite (Fig. 10d). The majority of the arkose data fall below the

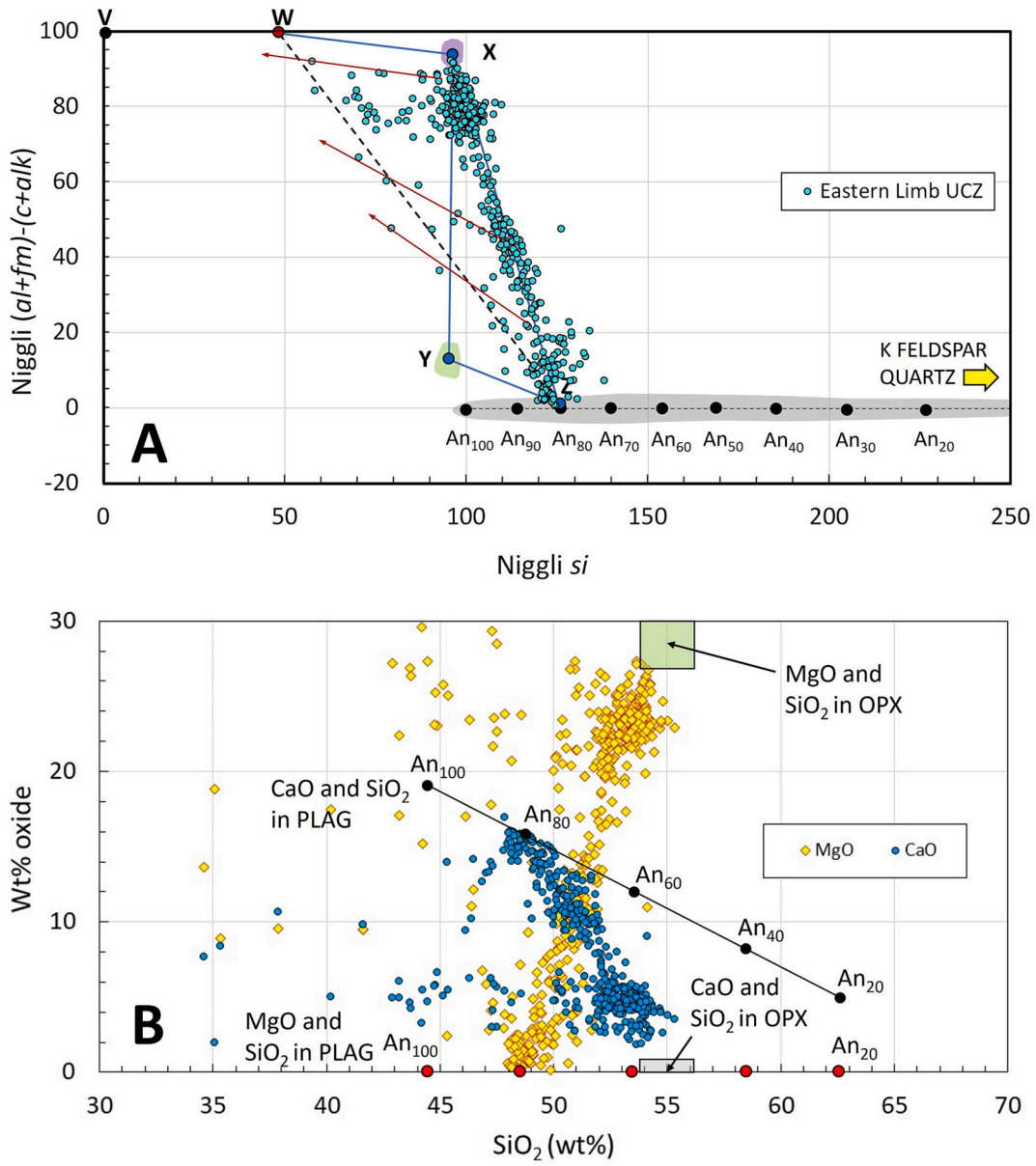

Fig. 6. (A) Niggli (*al* + *fm*)-(*c* + *alk*) versus *si* diagram with mineral nodes for spinel (V), olivine (W), orthopyroxene (X), clinopyroxene (Y) and plagioclase (Z) and data for the Upper Critical Zone of the eastern Bushveld Complex from Seabrook (2005); (B) Harker diagram showing MgO or CaO versus SiO_2 for the same Upper Critical Zone data. See text for further information.

igneous trend line as predicted, but have higher *mg* and/or *c* values than the original pelite field. While the precise interpretation of these sedimentary trends requires comparison with data on other Niggli plots, it is clear that they are very different from those described for igneous rocks above.

2.6. *si* versus *mg*

Leake and Singh (1986) have highlighted some of the many potential uses of the Niggli *si* versus *mg* plot. The fields for various common minerals are shown in Fig. 11a. Quartz plots at *mg* ~ 0 and *si* equal to infinity, giving an enormous potential range to data for very silica-rich rocks. Mafic silicates with Fe—Mg substitution define horizontal fields with narrow ranges of *si*. Olivine and chlorite cluster around 50, amphiboles and biotite around 75 and pyroxenes from 95 to 102. Carbonates and oxides plot at *si* = 0, with chromite and magnetite separated into distinctive fields along the *mg* axis. Plagioclase falls in a vertical field along *mg* = 0 and between *si* values of 100–300, and mixing lines between mafic silicates and plagioclase should follow curved trends (c.f. van de Kamp and Leake 1995), while ultramafic rocks comprising mixtures of olivine and orthopyroxene of similar Mg# can be assumed to lie on close to vertical trends and restricted to between the olivine and pyroxene fields. The calculated trend drawn in Fig. 11a for a model mixture of orthopyroxene (En_{81}) and plagioclase (An_{81}) are compared to real whole rock UCZ data from Seabrook (2005) in Fig. 11b. Samples with *si* values between 50 and 95 and falling on vertical trends should contain olivine. Data with *si* values >100 follow the model curve remarkably well but data sloping negatively away from the main trend (highlighted by red arrows) require an additional oxide component, as indicated by the vectors towards the chromite field (Fig. 11b).

When the *si* scale is expanded, the expected negative relationship between *si* and *mg* during igneous fractionation is demonstrated by the convergent margin volcanic rocks shown in Fig. 11c, while carbonate-rich alkaline rocks typically plot below the olivine field and across a wide range of *mg* values. Sedimentary rocks can show enormous variation in *si*; from near zero in carbonates to in excess of 10,000 in highly

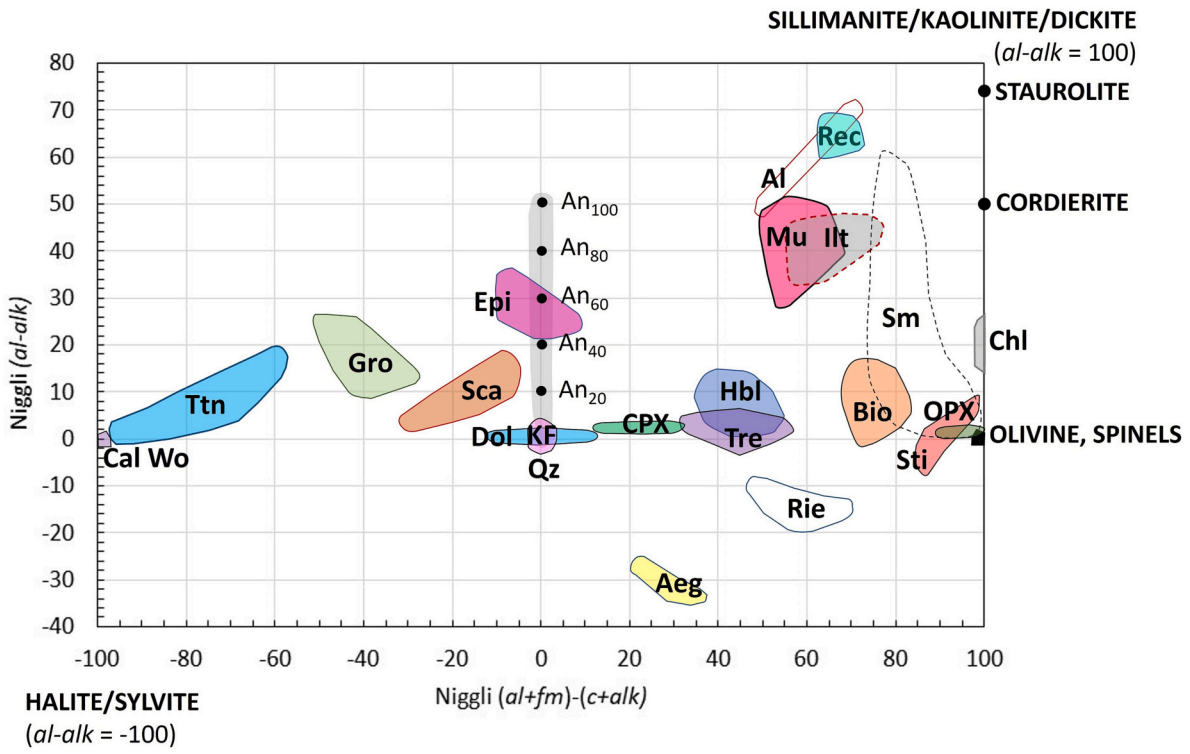

Fig. 7. Niggli (*al-alk*) versus (*al* + *fm*)-(*c* + *alk*) diagram with fields for common minerals shown. Abbreviations as in Fig. 1. Kaolinite, sillimanite, dickite, halite and sylvite plot outside the scale shown in the Figure, as indicated in the text. Data used to create the mineral fields are listed in Table 1.

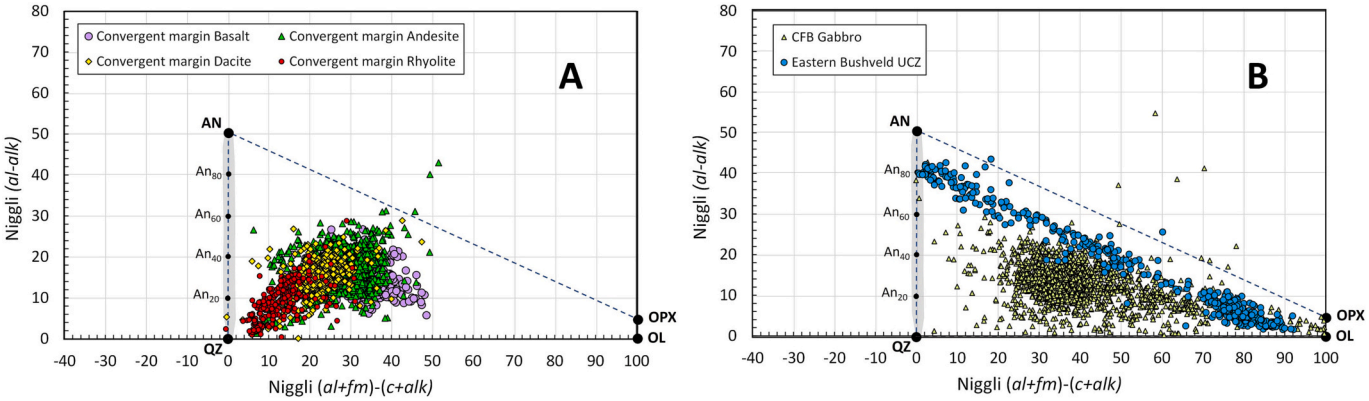

Fig. 8. Niggli (*al-alk*) versus (*al* + *fm*)-(*c* + *alk*) diagrams. (A) data for basalts, andesites, dacites and rhyolites from convergent margins; (B) data for Bushveld Upper Critical Zone and gabbros from Continental Flood Basalt provinces. Polygon for typical igneous rocks defined by OL (olivine), OPX (orthopyroxene), AN (anorthite) and QZ (quartz). Data sources are listed in Table 1.

mature quartz arenites (Niggli, 1954). Quartz and feldspar contain little or no Mg relative to Fe and fall on the left hand side of the plot. As such, the observed range and variation in *mg* for most clastic sedimentary rocks (0.3–0.7) are controlled by clays, mica, chlorite and detrital Fe oxides or other ferromagnesian silicates. As noted by Leake and Singh (1986), only sedimentary rocks containing dolomite are expected to produce negative trends towards higher *mg*; as exemplified by a small number of the Colorado siltstones (Fig. 11d) that also plot in or close to the dolomite field in *ca* versus *mg* space in Fig. 10d.

3. Case studies demonstrating applications of Niggli Numbers

3.1. Case Study 1 – Evolution of a layered intrusion; Rustenburg Layered Suite, Bushveld Complex

As shown in Sections 2.5 and 2.6, the Niggli Number calculation can produce highly restricted values for parameters like *si*, *c* or *al-alk* for entire groups of minerals such as olivine, pyroxenes or amphiboles, regardless of the Fe/Mg ratio in the mineral and the extent of fractionation. This is a real advantage when compared to plotting oxide concentrations of major elements where SiO_2 or FeO can occupy a wide range of values in the same silicate mineral depending on fractionation. On diagrams where Niggli Numbers or sums are plotted against an independent parameter such as stratigraphic height, lines or narrow boxed fields can consistently and elegantly represent a given mineral at any

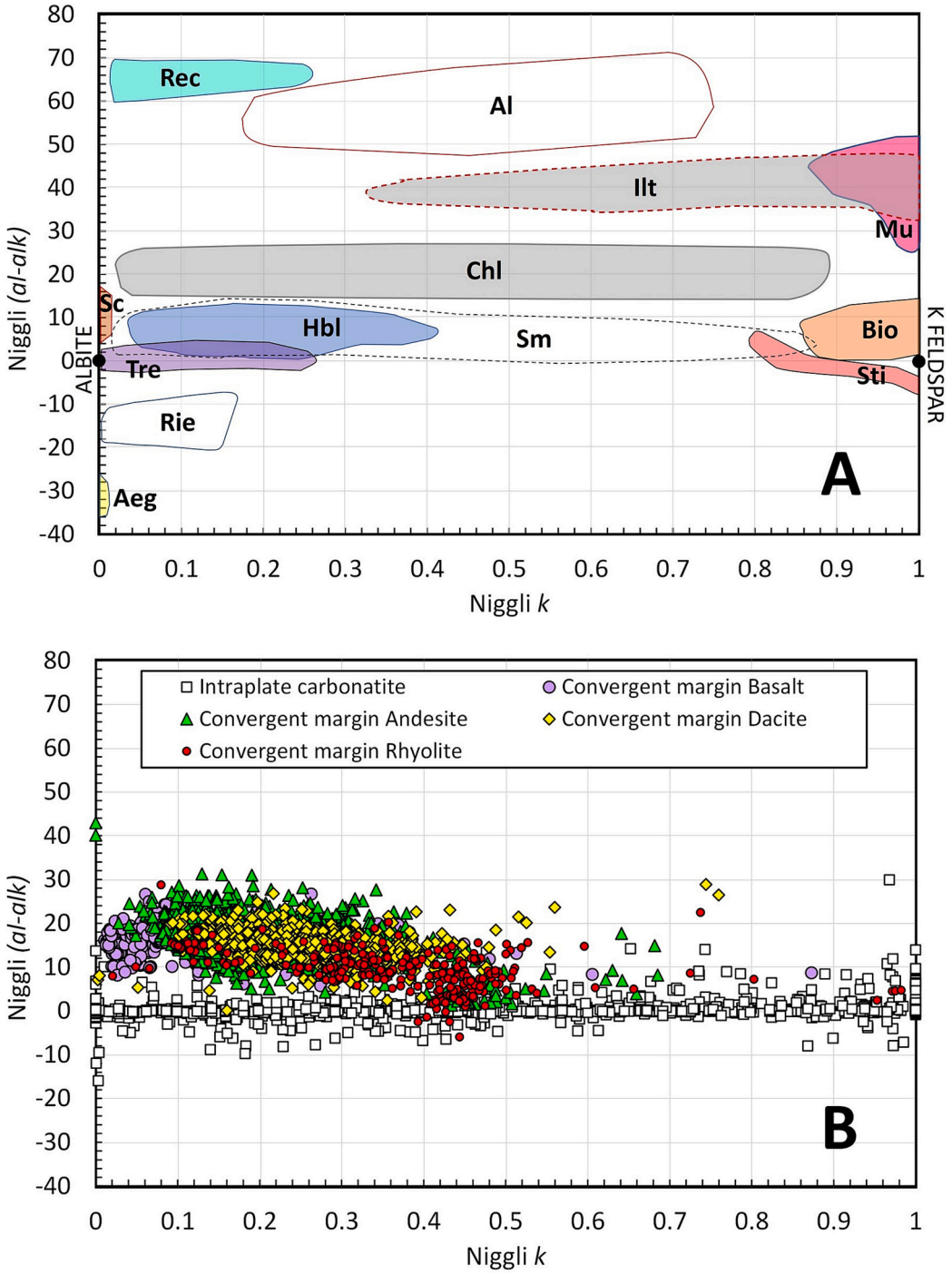

Fig. 9. Niggli (*al-alk*) versus *k* diagrams: (A) fields for selected alteration minerals with abbreviations as in Fig. 1.; (B) data for basalts, andesites, dacites and rhyolites from convergent margins and intraplate carbonatites. Data sources are listed in Table 1.

point in the crystallization history of an intrusion. Whether Niggli data plot close to, between or outside the fields of certain minerals can reveal important petrological information and using a number of simple rules it is possible to make an intuitive interpretation of the major minerals that must be present in the sequence. The potential of this approach for any large intrusion with variable mineralogy is illustrated using the stratigraphy of the Rustenburg Layered Suite (RLS; South African Committee for Stratigraphy, 1980) of the 2.06 Ga Bushveld Complex of South Africa.

Geographically, the RLS is subdivided into 5 limbs: far western, western, eastern, northern and the southern (Bethal) limb that is largely obscured by cover rocks. The RLS is intruded into the metasediments of the Transvaal Supergroup but this occurs at different stratigraphic levels for different limbs. In the eastern and western limbs, the mafic magmas mostly intrude the quartzites and siltstones that comprise the upper portions of the early Proterozoic (2.5–2.1 Ga) Pretoria Group. Stratigraphically the RLS is conventionally divided into five zones, comprising in sequence: a Marginal Zone of norites; Lower Zone (LZ) pyroxenites and harzburgites; Critical Zone chromitite-pyroxenite-norite cyclic units; Main Zone (MZ) gabbronorites; and Upper Zone (UZ) anorthosites, gabbros and magnetitites (Eales and Cawthorn, 1996).

Fig. 12 shows a *si* versus *mg* plot for all of the zones of the RLS on a

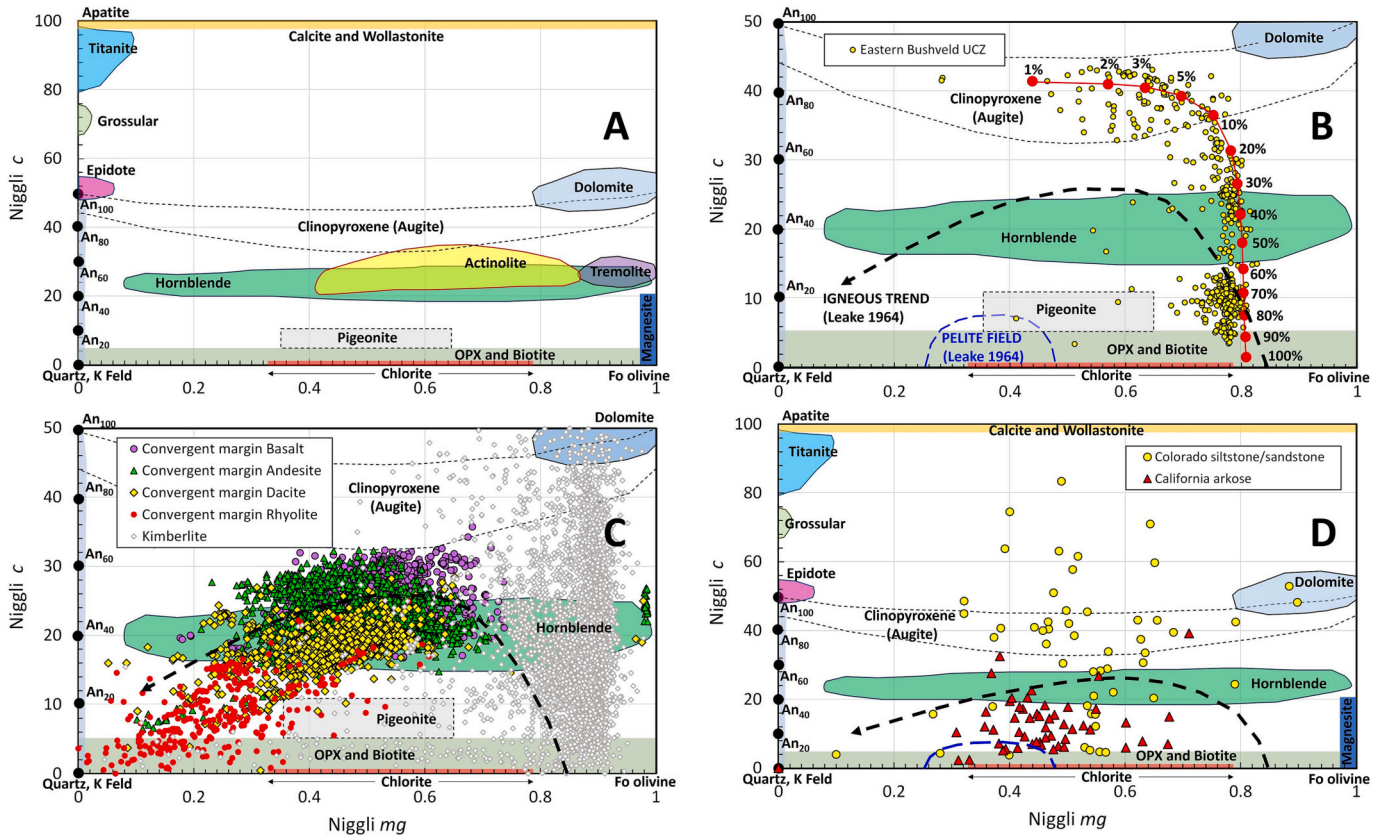

Fig. 10. Niggli *c* versus *mg* diagrams: (A) fields for common minerals; (B) lower portion of the diagram up to $c = 50$ showing a model mixing trend between En_{81} and An_{81} (red dashed line with the percentage of pyroxene in the rock shown at various points) compared to Upper Critical Zone data and the igneous trend and pelite field defined by Leake (1964); (C) data for basalts, andesites, dacites and rhyolites from convergent margins compared to the Leake (1964) igneous trend; (D) Siltstones and sandstones from Colorado and California arkose samples. Data sources are listed in Table 1. See text for more information. (For interpretation of the references to colour in this figure legend, the reader is referred to the web version of this article.)

single diagram. The majority of LZ rocks lie between the olivine and pyroxene lines at *mg* values >0.8 whereas the olivine-bearing portions of the UCZ have *mg* < 0.8. Plagioclase-bearing rocks of the Critical and Main zones fall on trends similar to the model curve shown in Fig. 11a with *mg* values between 0.50 and 0.75. Primitive portions of the UZ fall on the same trend as the MZ but at *mg* values <0.50, the UZ data form a cone-shaped data cloud. Divergence above or below the previous trend is a function of the presence or absence of magnetite in a given UZ sample and composition and the amount of plagioclase relative to ferromagnesian minerals.

Fig. 13 displays a composite stratigraphic and Niggli geochemical profile constructed using data from the western limb for the Lower and Lower Critical zones (Teigler and Eales, 1996), and from the eastern limb for the Upper Critical, Main and Upper zones (Seabrook, 2005; Lundgaard et al., 2006; Vantongeren et al., 2010; Setera and VanTongeren, 2018). The pyroxenite Merensky Reef (MR) of the UCZ serves as a common reference horizon for both limbs and the stratigraphic distance above or below this horizon is shown as the vertical scale in Fig. 13. Following Kruger (2005), for the purpose of this example, the stratigraphic boundary between the Main and Upper zones is taken as the Pyroxenite Marker (PXM).

The Niggli *si* diagram in Fig. 13 shows vertical mineral fields for spinels, olivine and pyroxenes and variable values of *si*, *c* and (*al-alk*) for plagioclase. The *si* values for the Lower and Lower Critical zones are typically 100 or less. Values close to 100 would be expected to be pyroxenites whereas values 50–100 require more silica-poor components (mostly likely olivine but possibly also spinel), and any samples with *si* values <50 must contain spinel (chromite). Small amounts of interstitial plagioclase in some samples are suggested by *c* values >4 and (*al-alk*) values >3, the maximum values for LZ and LCZ orthopyroxene. The frequency and abundance of plagioclase increases with height in the LCZ. The majority of UCZ and MZ samples are typified by *si* > 100 and *c* > 5, which requires significant plagioclase in addition to any ferromagnesian minerals. Drops in *si* to ~100 indicate pyroxenite horizons, and both the Merensky Reef and Pyroxenite Marker are clearly identifiable by matching decreases in *si* and *c*. Rising maximum *si* values in the UZ require increasingly Na-rich plagioclase (and/or quartz) and any decrease in *si* below 100 must reflect the presence of significant magnetite and/or Fe-rich olivine. Magnetite is clearly tracked and distinguished from olivine (which will not accommodate Ti) using the Niggli *ti* diagram where it is obvious that high *ti* values indicating the appearance of magnetite are restricted to the Upper Zone (Fig. 13).

The *c* and (*al-alk*) profiles are best compared in conjunction, as closely matching profiles indicate that plagioclase is crystallizing alone, without significant clinopyroxene. In the absence of clinopyroxene, corresponding maxima on both *c* and (*al-alk*) profiles (as well as on *si*) identify the most plagioclase-rich rocks, and the observed maximum value of *c* or (*al-alk*) can be projected to estimate the An content of plagioclase in these anorthosites and leuconorites. This situation holds for the UCZ and lowermost portion of the MZ but above +250 m, the trends for *c* and (*al-alk*) diverge and move in opposing directions, reflecting increasing influence from clinopyroxene in the MZ that buffers *c* while at the same time lowering (*al-alk*). From this point it is not possible to infer plagioclase composition from the maximum *c* or (*al-alk*) values. On the *mg* plot there is a negative offset (both in terms of maximum values and range) between the UCZ and the MZ that mirrors small positive offsets on both the *si* and *ti* plots. These shifts are likely to be related to the new magma influx inferred to have taken place around

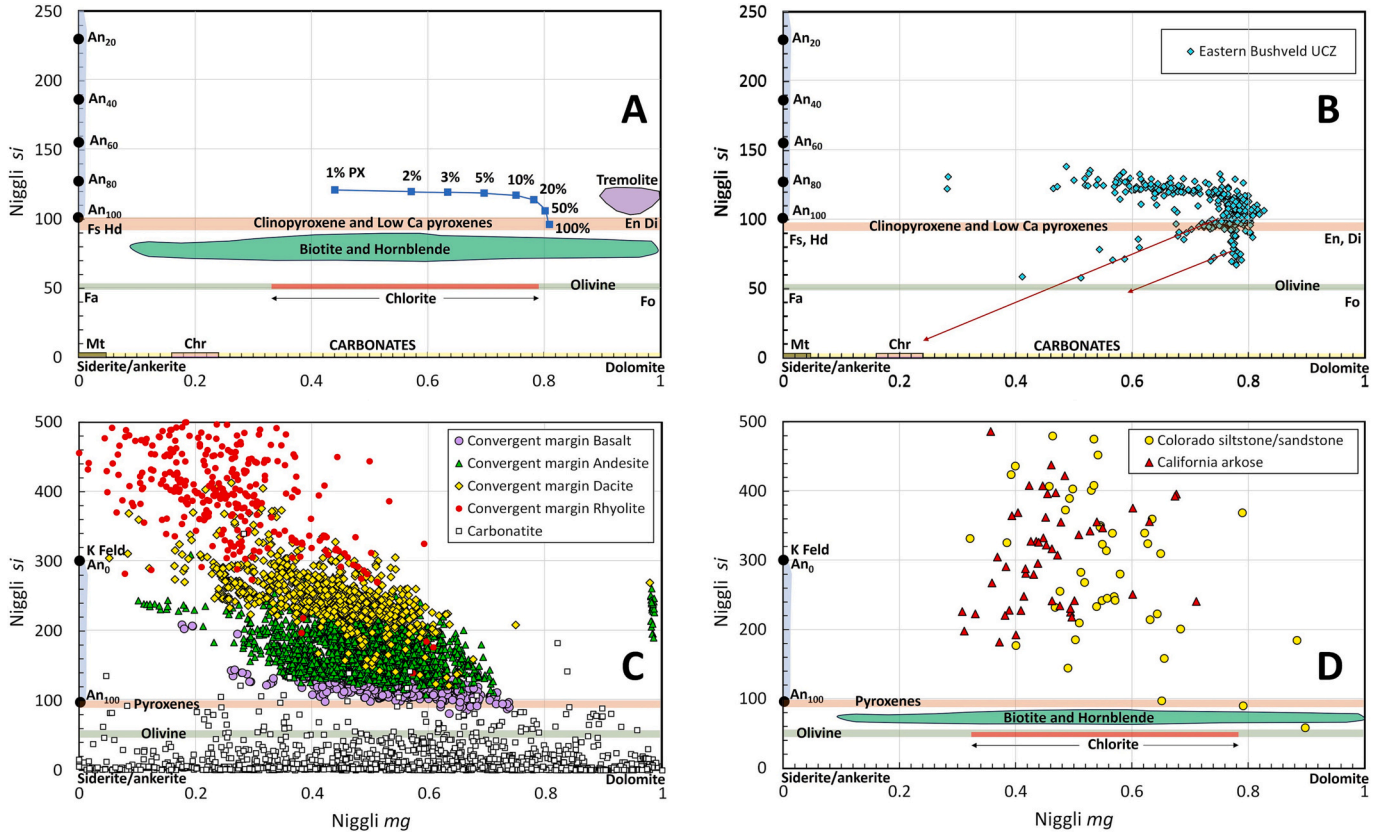

Fig. 11. Niggli *si* versus *mg* diagrams: (A) fields for common minerals in mafic rocks with a model mixing trend between En_{81} and An_{81} (blue line with the percentage of pyroxene shown); (B) eastern Bushveld Upper Critical Zone data with vectors indicating chromite-bearing rocks shown by red arrows; (C) data for basalts, andesites, dacites and rhyolites from convergent margins and intracraton carbonatites; (D) Siltstones and sandstones from Colorado and California arkose samples. Data sources are listed in Table 1. Additional mineral abbreviations En (enstatite), Di (diopside), Fs (ferrosillite), Hd (hedenbergite). See text for more information. (For interpretation of the references to colour in this figure legend, the reader is referred to the web version of this article.)

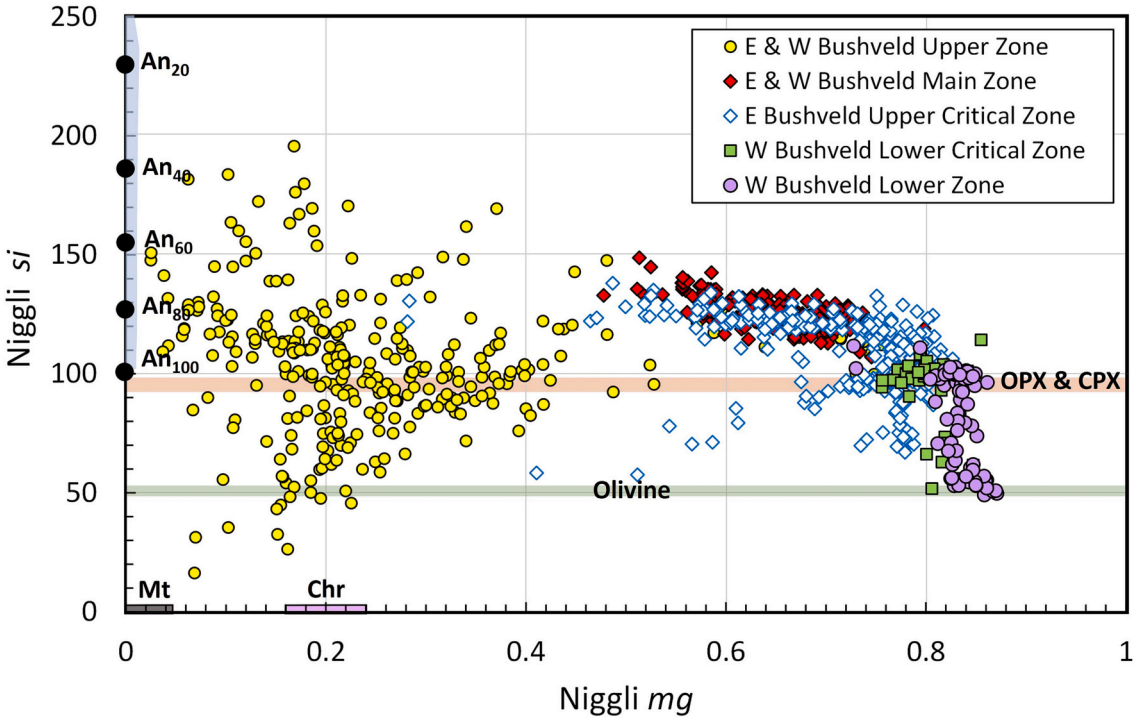

Fig. 12. Niggli *si* versus *mg* diagram for the different zones of the RLS of the Bushveld Complex. Data sources are listed in Table 1. See text for more information.

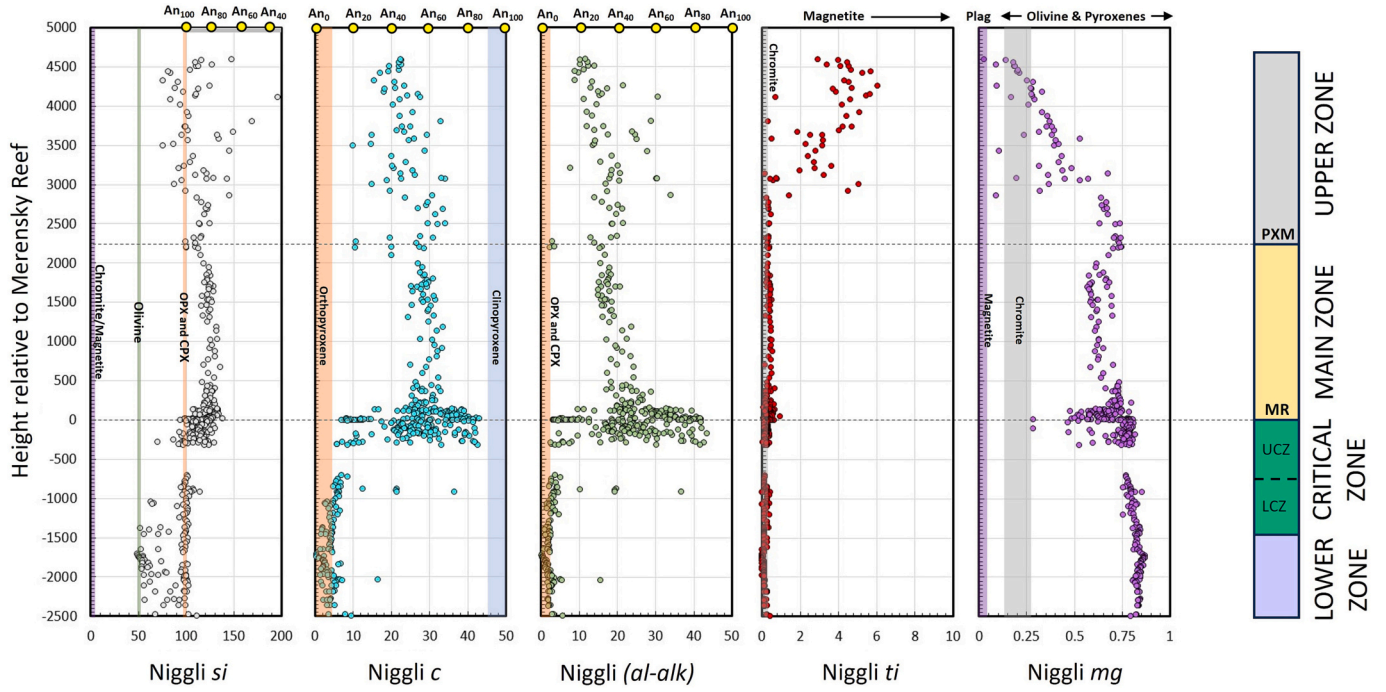

Fig. 13. Stratigraphy for the Rustenburg Layered Suite (RLS) of the Bushveld Complex combined with Niggli Number profiles. Mineral fields relevant to different numbers, ratios or sums are shown on the relevant profile. Data sources are listed in Table 1. See text for more information.

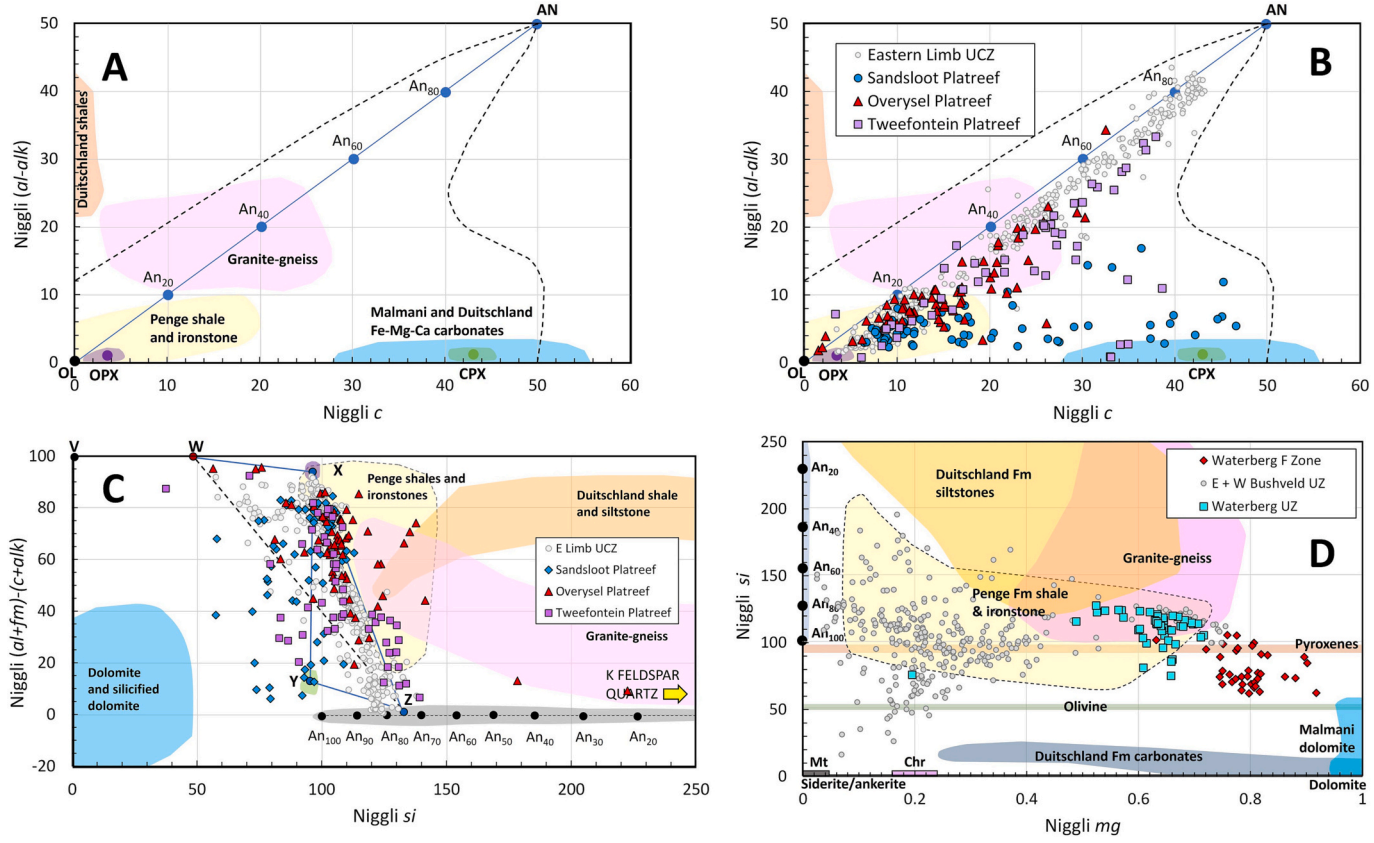

Fig. 14. Niggli plots for the RLS and various country rocks from the northern limb of the Bushveld Complex: (A) (*al-alk*) versus *c* plot for country rocks; (B)) (*al-alk*) versus *c* plot for Platreef/Critical Zone mafic rocks and country rocks; (C) (*al* + *fm*)-(*c* + *alk*) versus *si* plot for Platreef/Critical Zone mafic rocks and country rocks; (D) *si* versus *mg* plot for Upper Zone rocks from the eastern and western Bushveld compared to F Zone and proposed Upper Zone rocks from the Waterberg Project. Data sources are listed in Table 1. See text for more information.

the level of the Merensky Reef (Kruger 2005). From the above, it is clear that, even assuming no prior knowledge of the RLS and simply interpreting the whole rock data at face value, the Niggli profiles allow enormous amounts of useful petrological information to be extracted quickly and intuitively. This approach should be similarly applicable to other layered intrusions where sufficient major element data and data coverage exist.

3.2. Case Study 2 – Tracing magma contamination and mineralization; Northern Bushveld Complex

In the northern limb, the RLS is intruded into stratigraphically older and more chemically reactive country rocks than for the eastern and western limbs. These country rocks comprise the shales, carbonates and banded iron formations of the late Archaean (2.7–2.5 Ga) Chuniespoort Group and the underlying Archaean granite-gneiss and greenstone basement. The contact interval between the RLS and country rocks, termed the Platreef (White, 1994; McDonald and Holwell, 2011), contains significant Ni-Cu-PGE sulfide mineralization and the mafic magma intrudes progressively into stratigraphically older rock units along strike to the north. The Platreef interval has been suggested to be the stratigraphic equivalent of the Upper Critical Zone in the eastern and western limbs (White 1994; Yudovskaya et al., 2017; Grobler et al., 2019) but this has not been established unambiguously (Kinnaird and McDonald, 2018).

Niggli Numbers for the major country rocks were calculated and fields for each major lithology are coloured coded and shown in Fig. 14a. The plots in Fig. 14b and c compare eastern limb UCZ rocks with Platreef/Critical Zone rocks from three adjacent localities where the mafic rocks are known or suspected to interact with different mixtures of country rocks (Buchanan et al., 1981; Armitage et al., 2002; McDonald et al., 2005; Nex, 2005; Holwell and McDonald, 2006; Ihlenfeld and Keays, 2011). At Tweefontein, the mafic magmas mostly interact with Penge Formation ironstones and shales and Malamani Formation dolomites; at Sandsloot with Malmani dolomites; and at Overysel with Malmani dolomites and Archaean granite-gneiss basement.

The eastern limb UCZ data plot close to the plagioclase line, as discussed in Section 2.2. While some Platreef data from each locality also parallel the plagioclase line (albeit offset right to consistently higher *c* values than the majority of UCZ samples), a significant fraction of the data deviates from the line and trends towards one or more of the country rocks (Fig. 14b). On the (*al* + *fm*)-(*c* + *alk*) versus *si* diagram in Fig. 14c, all three localities display Platreef data outside the olivine-plagioclase-orthopyroxene and plagioclase-orthopyroxene-clinopyroxene polygons. Tweenfontein data lie towards the dolomite field and also right of the plagioclase-orthpyroxene tie line into the silica-rich fields occupied by ironstone and granite. Many Sandsloot samples lie left of the olivine-plagioclase and pyroxene linestowards the dolomite field. The converse is true for the Overysel data where no data plot left of the olivine-plagioclase and pyroxene lines but many data points plot to the right of plagioclase-orthopyroxene line in the granite-gneiss field (Fig. 14b).

A different example can be illustrated using *si* versus *mg* for the mineralized and unmineralized mafic-ultramafic rocks at the Waterberg Project located at the far northern end of the northern limb. The geology and geochemistry of this sequence have been described by Kinnaird et al. (2017) and Huthmann et al. (2018) but two features are highlighted here. Above a (<100 m thick) basal ultramafic sequence, is a troctolite-gabbronorite-anorthosite sequence that is up to 850 m thick and which Kinnaird et al. (2017) have suggested to correlate with the Main Zone elsewhere in the northern limb. The lower part of this sequence is characterized by a complex zone of olivine-orthopyroxene-plagioclase cumulates containing Ni-Cu-PGE mineralization known as the Waterberg F Zone. Above the troctolite-gabbronorite-anorthosite sequence, up to 150 m of ferrogabbro and magnetite gabbronorite may be present below an erosional contact with overlying Waterberg Group sedimentary rocks and both McCreesh (2016) and Kinnaird et al. (2017) have suggested, based on the occurrence of disseminated magnetite, that these ferrogabbros may be equated with the Upper Zone. It is important to note that no Transvaal Supergroup sedimentary rocks outcrop or have been reported in the Waterberg Project area and, unlike in the Platreef and other portions of the northern limb, no large metasedimentary rafts or xenoliths have been recorded from the available drill cores (Kinnaird and McDonald, 2018).

Fig. 14d shows data from the F Zone and the proposed Upper Zone at Waterberg compared with country rocks and Upper Zone data from the eastern and western limbs in *si* versus *mg* space. The carbonate rocks of the Malmani and Duitschland formations have different Mg/Fe ratios and degrees of silicification and are usefully separated on this plot. The majority of the F Zone data plot between the olivine and pyroxene lines but instead of falling on near vertical trends with a narrow range of *mg* values (c.f. the UCZ data in Fig. 11b) that are consistent with the observed Mg/Fe of olivine and pyroxene ($Mg\#_{65–75}$; McCreesh, 2016) the data are widely dispersed and skewed towards higher *mg*. Five F Zone data points lie at even higher *mg*, separated from the main data cluster and vectoring towards the dolomite field. These features strongly suggest that there is a cryptic Mg-rich and silica-poor component in the F Zone rocks, most likely derived from assimilation of dolomite. Most of the Waterberg Upper Zone data follow a trend above the pyroxene line that is similar to the most primitive portion of the conventional Upper Zone. However a subset of the Waterberg data define near-vertical vectors towards much lower *si* (Fig. 14d). Some of these plot between the olivine and pyroxene lines despite the general absence of olivine observed in thin section by McCreesh (2016). These data suggest that either olivine may be more widespread than previously recognised, or that the ferrogabbros contain an additional silica-poor component, possibly similar to the Duitschland formation carbonates. Collectively, these findings suggest that there were sedimentary country rocks (likely including Lower Transvaal carbonates of the Chuniespoort Group) in the area where the Waterberg Project mafic magmas intruded, but these were so effectively assimilated that only cryptic chemical evidence remains for their former presence.

Niggli Numbers can also be used to quickly and effectively represent whether mineralization is hosted by lithologies likely to be igneous or hybrid/non-igneous. Fig. 15a shows data for the Merensky Reef and its associated Merensky Cyclic Unit taken from the eastern limb (Wilson and Chunnett, 2006) expressed in (*al-alk)* versus *c* space but with symbols and colours classified by combined Rh + Pt + Pd + Au grade. Both barren and grade-bearing samples occur close to and parallel with the plagioclase line. The majority of high grade samples are pyroxenites or melanorites, but examples of high grade norite and leuconorite are also evident. Fig. 15b shows similar data, classified according to Rh + Pt + Pd + Au grade, for an exploration borehole (designated X) collared at an unspecified locality in the northern limb. The distribution of intermediate and high grade samples is not as closely tied to the plagioclase line and a large fraction of the strongly mineralized samples track towards dolomite and the field of clinopyroxene. In the same manner, contamination predominantly by clay-rich sediments would be expected to move the distribution to the left of the plagioclase line towards the brown shale field. It is clear that the slope between (*al-alk*) and *c* and its proximity to 1 (representing buffering by idealised plagioclase) has significance for contamination and potential mineralization. Most intermediate and high grade samples in Borehole X have (*al-alk*)/*c* values <0.5, whereas most barren or low grade samples are >0.5 (Fig. 15b). This is a more rigorous and illustrative tool than attempting to assess carbonate contamination using assumed degrees of variation in whole rock CaO/Al_2O_3 ratios, as has been adopted in previous studies (e.g. Harris and Chaumba, 2001; Kinnaird, 2005; Holwell et al., 2007).

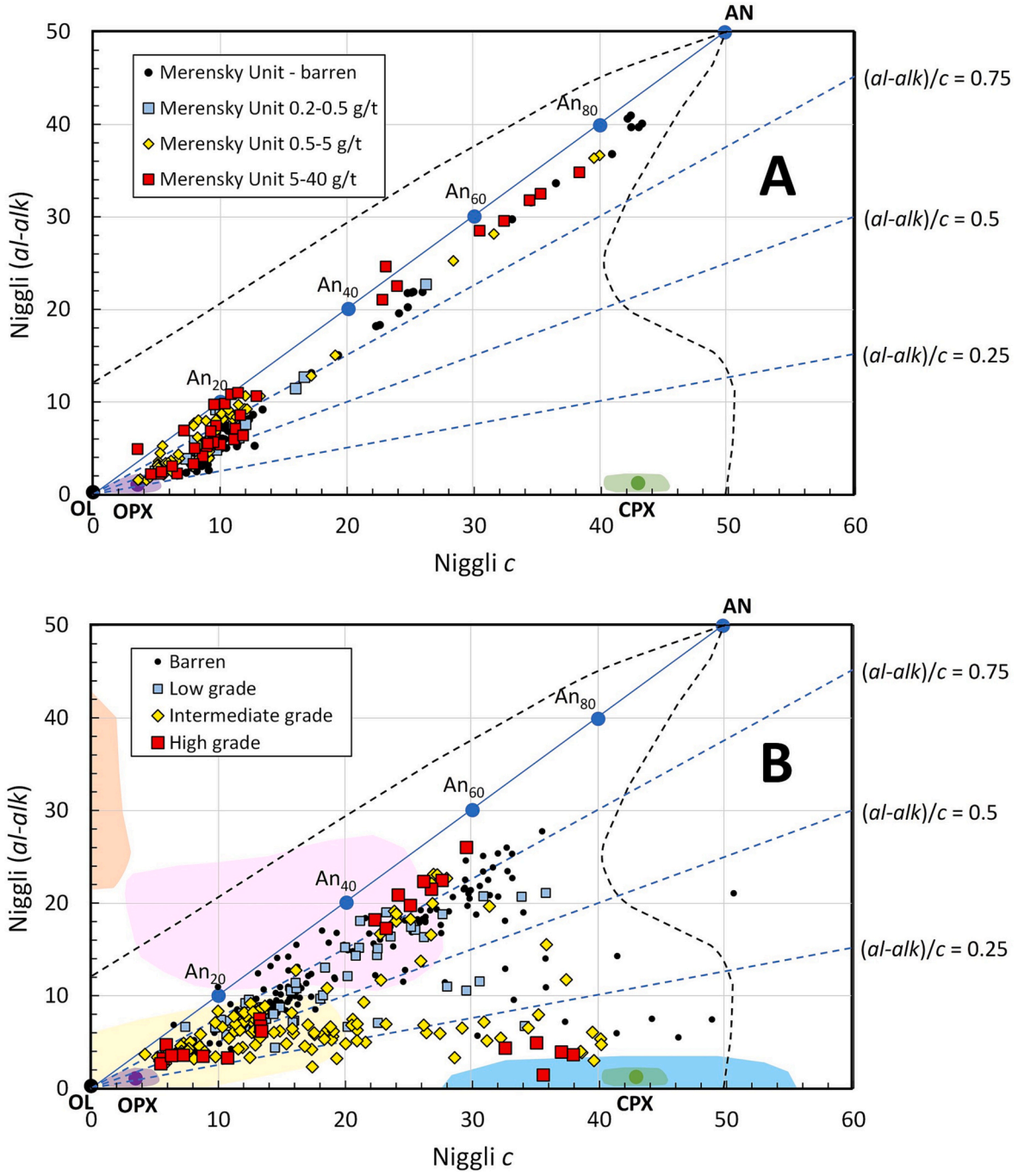

Fig. 15. Niggli (*al-alk*) versus c plots with data classified by PGE + Au grade (barren, low, intermediate and high): (A) Merensky Reef and Merensky cyclic unit from Wilson and Chunnett (2006); anonymised grade data from northern Bushveld borehole X.

3.3. Case Study 3 – Geochemical tracers for hydrothermal alteration

The Niggli diagrams presented in Section 2 contain fields for secondary minerals that may develop during hydrothermal alteration linked to the formation of mineralization in Cu-Pb-Zn volcanogenic massive sulfide (VMS) deposits, Cu—Mo porphyry systems, or epithermal Au—Ag silver deposits. The review by Mathieu (2018) lists a number of methods - each with associated advantages and disadvantages - that may be applied to characterizing the type, and quantifying the extent, of alteration using bulk geochemical data. These include various alteration indices, such as the Ishikawa alteration index (IAI; Ishikawa et al., 1976) and the chlorite-carbonate-pyrite index (CCPI; Large et al., 2001) calculated from major element data, as well as methods based on calculations of normative mineralogy. In addition, the GER methods outlined by Stanley (2020) provide a means of identifying the development of, and the influence exerted, by particular alteration minerals.

The simplicity and flexibility of the Niggli method, and the consistent framework in which suites of rocks can be represented in relation to minerals on binary diagrams offers an additional set of tools with which to complement these existing methods. This is illustrated using Niggli plots in Fig. 16 for the chloritization case study from Mathieu (2018) based on major element data for the Hongtoushan VMS deposit in China, published by Zheng et al. (2013). Interestingly, the latter authors calculated and plotted Niggli (*al-alk*) and *c* values for the least altered volcanic rocks to establish that they plotted in the field for typical

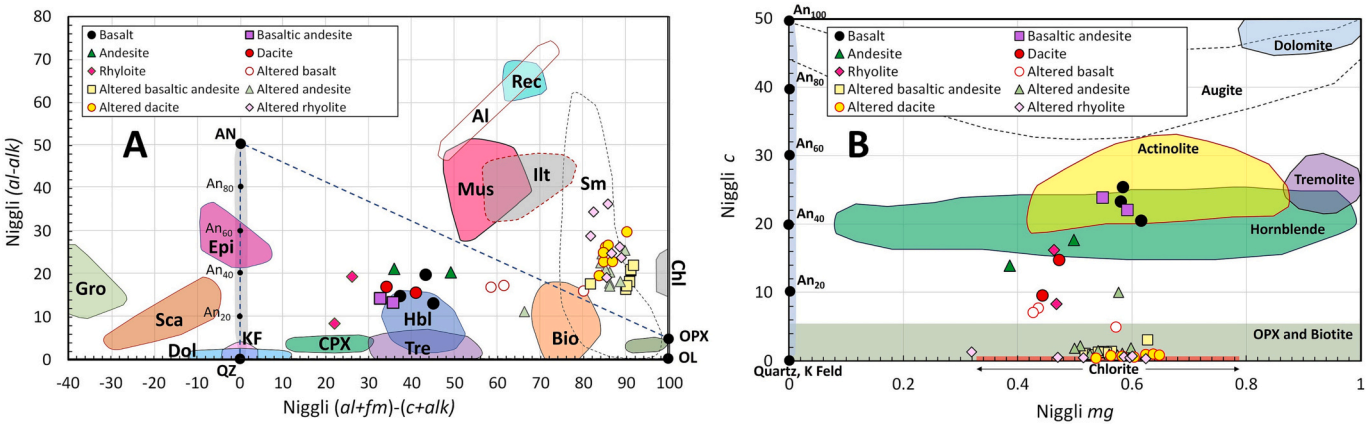

Fig. 16. Fresh and altered volcanic rocks from the Hongtoushan VMS deposit expressed on the (*al-alk*) versus (*al* + *fm*)-(*c* + *alk*) diagram (A) and the *c* versus *mg* diagram (B). Data from Zheng et al. (2013). Abbreviations as in Fig. 1.

igneous rocks (Fig. 1). However they did not plot any Niggli Numbers for the altered rocks. Fresh and altered volcanic rocks are compared using the (*al-alk*) versus (*al* + *fm*)-(*c* + *alk*) plot in Fig. 16a and using the *c* versus *mg* plot in Fig. 16b. The least altered volcanics fall in the expected field for igneous rocks (OL-OPX-AN-QZ) and clearly are separated from the chloritized rocks which plot at consistently higher (*al* + *fm*)-(*c* + *alk*) values. All but three of the chloritized rocks lie outside of the igneous field and the majority plot near the end of a line drawn between the fresh volcanic data cluster and the chlorite field. In *c* versus *mg* space, the least altered rocks fall on an anticlockwise fractionation arc similar to that generally shown by convergent margin volcanics in Fig. 10c. The altered rocks are shifted towards lower *c* values and also higher *mg* values in the case of most of the altered felsic rocks. The altered data cluster along the bottom of the plot, within or close to the chlorite field (Fig. 16b). The Hongtoushan example demonstrates the utility of these Niggli plots for representing the chloritization alteration style clearly and effectively.

Alteration effects, involving development of chlorite-sericite-biotite-carbonate, for the Mathieu (2018) case study based on the Le Grande Sud intrusion in Quebec (Mercier-Langevin, 2000) are more subtle. Comparing altered rocks with sample 19,449, that was assumed by Mercier-Langevin (2000) to be the least altered, revealed moderate losses of Na and gains in K, with only overall enrichment in Mg and Fe associated with chloritization (Mathieu 2018). Niggli Numbers calculated from data in Mercier-Langevin (2000) are shown on the (*al-alk*) versus (*al* + *fm*)-(*c* + *alk*) plot in Fig. 17a and on the (*al-alk*) versus *k* plot in Fig. 17b. Compared to the least altered sample, positive shifts to higher (*al* + *fm*)-(*c* + *alk*) and *k* are recorded by parts of the data. The cluster of altered points that lie to the left of sample 19,449 in Fig. 17a define a trend towards calcite at (*al* + *fm*)-(*c* + *alk*) = 100 (c.f. Fig. 7).

Different parts of porphyry Cu—Mo hydrothermal systems may be subject to the effects of phyllic, argillic, propylitic and potassic alteration (Seedorff et al., 2005) and these are tested and illustrated using filtered data from the dataset for intrusive rocks of northern Nevada compiled by du Bray et al. (2022). Data for fresh dacites and granodiorites (filtered for <1.5 wt% LOI) compared to dacites and granodiorites recorded in the database as affected by phyllic, argillic, propylitic or potassic alteration are shown on Niggli (*al-alk*) versus (*al* + *fm*)-(*c* + *alk*) and (*al-alk*) versus *k* plots in Fig. 18. Dacites and granodiorites experiencing phyllic or argillic alteration are separated from the fresh rocks and plot within, or define trends towards, the muscovite and clay (primarily illite) fields on both Niggli plots. Granodiorites subjected to potassic alteration are partly separated from the fresh rocks, with most samples shifted towards greater (*al* + *fm*)-(*c* + *alk*) values and *k* values that track towards biotite (and muscovite). But this is not universal and a small number of samples apparently classified as potassic actually have lower *k* than the fresh rocks (Fig. 18d), suggesting that they should be re-examined and potentially re-classified in the database.

For the dacites and propylitic altered dacites (Fig. 18a and b), data plot nearly on top of each other illustrating that this alteration style is largely isochemical with respect to the elements involved in the Niggli calculation. The picture is similar for most propylitic granodiorites but a subset of these have elevated (*al-alk*) and define an apparent trend towards muscovite and illite on Fig. 18c but have correspondingly very low *k* values (Fig. 18d). This paradoxical outcome suggests that the cause for this cannot be sericitization but some other process involving removal of Ca relative to Al and K relative to Na.

The case studies based on known alteration styles detailed above illustrate how Niggli Numbers may be used as an additional geochemical tool alongside conventional alteration indexes or normative calculations to infer alteration style(s) from major element data. These data are typically generated during the early phases of mineral exploration, when the extent and characteristics of a hydrothermal system (including its metal potential) may be poorly known. The data needed for the Niggli calculation are relatively cheap and can be generated rapidly. This means that interpretations based on Niggli plots can be used prior to or alongside slower and more expensive studies on fluid inclusions or the trace element chemistry of minerals to help track alteration.

3.4. Case Study 4 – Chemical stratigraphy of sedimentary sequences

Chemical stratigraphy (or chemostratigraphy) is a technique that relies on inorganic bulk rock and mineral analysis that is often used alongside lithostratigraphy, magnetostratigraphy and biostratigraphy for determining the stratigraphic relations within and between sequences in sedimentary basins (Craigie, 2018). Chemostratigraphy can be applied to mudstones, siliciclastic and volcaniclastic sediments and carbonates, and is particularly useful for continental sediments where sequences are oxidised or where a low frequency of macro- or microfossils severely limits any biostratigraphic correlations (Pearce et al., 1999; Ramkumar et al., 2021; Ravidà et al., 2023) or in Precambrian sedimentary sequences where fossils are effectively absent (Frimmel et al., 2006). Whole rock and/or mineral data are represented as profiles that display variations with depth, following workflows similar to those described in Craigie (2018). It has long been recognised that element concentrations on their own may be sensitive to the effects of grain size and a common approach is to minimize this by creating profiles normalized to Al, to account for the clay fraction of the rock (Pearce et al., 2005; Craigie et al., 2016). Principal component analysis is commonly used to further identify major groupings of elements and further regression analysis carried out to determine element correlation and illustrate element associations with particular minerals. Trace element ratios and discrimination plots may also be used to represent

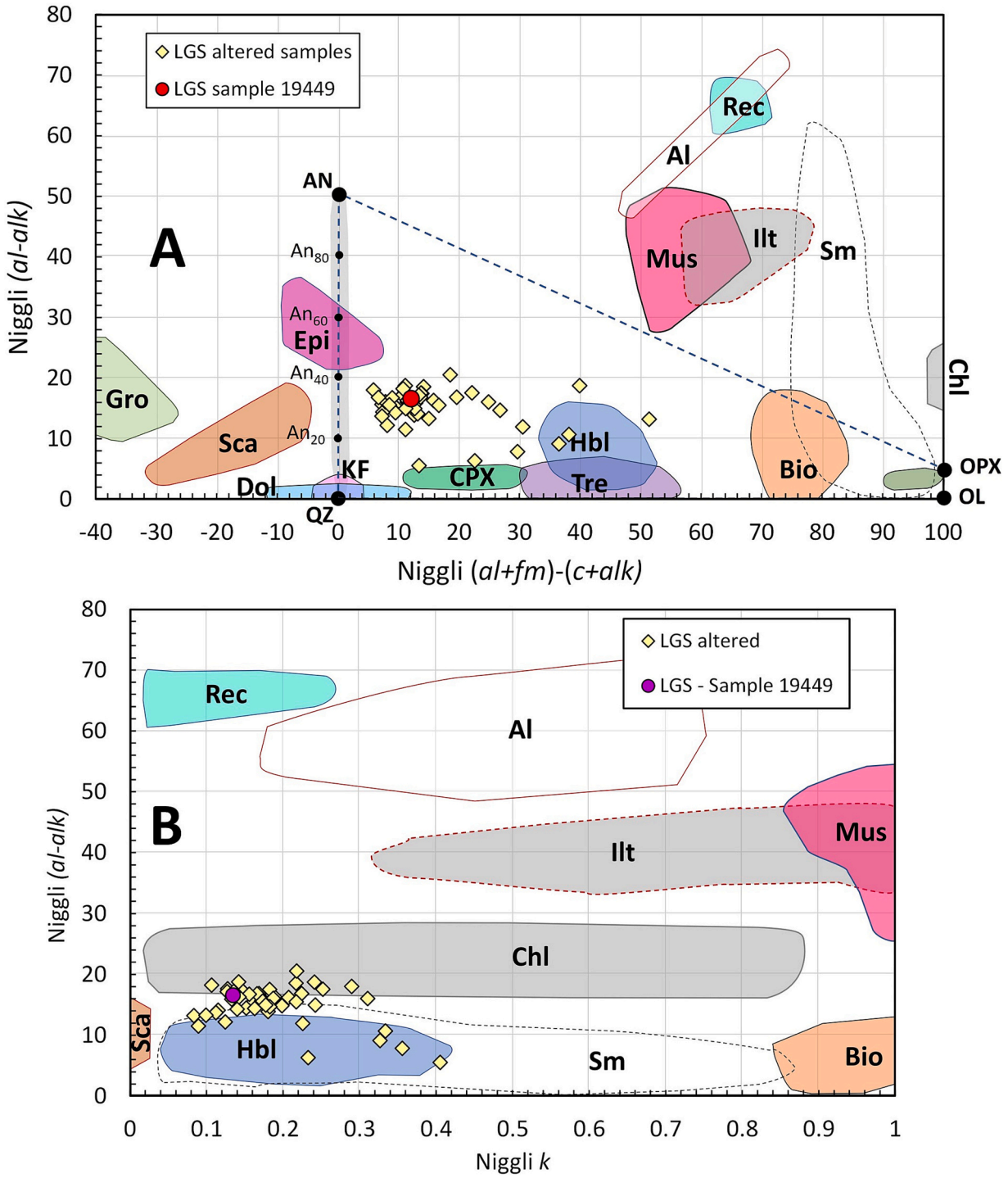

Fig. 17. Altered samples (yellow diamonds) from the Le Grande Sud intrusion plotted on the Niggli (*al-alk*) versus (*al* + *fm*)-(*c* + *alk*) diagram (A) and the (*al-alk*) versus *k* diagram (B) and compared to sample 19,449 (red dot) that is assumed to be the least altered sample. Data from Mercier-Langevin (2000). Abbreviations as in Fig. 1. (For interpretation of the references to colour in this figure legend, the reader is referred to the web version of this article.)

and determine any changes in provenance within an evolving sedimentary basin (Ramkumar et al., 2021). Finally, the profiles of selected major and trace element ratios are used to create a chemostratigraphic interpretation for a borehole or well. This interpretation is based on a hierarchical structure composed of major zones (sometimes referred to as chemozones), subzones, divisions and subdivisions that may be reflected in whole, or in part, in other wells or boreholes that intersect the sequence (Craigie, 2018; Ravidà et al., 2023).

In principle, Niggli Numbers should serve as a complimentary tool within this established approach as they track mineralogy, or the combination of minerals, very successfully and ought to aid both in assigning lithologies and highlighting internal changes within a wider stratigraphic unit. The primary Niggli Numbers collectively encompass the chemical building blocks of all common carbonates, evaporites, feldspars, micas, clays and detrital ferromagnesian minerals. Secondary numbers like *si* and *p* directly track the proportion of quartz and phosphate, while *ti* will also track detrital minerals. As discussed in Section 2, because secondary numbers like *si* are unbounded in terms of scale

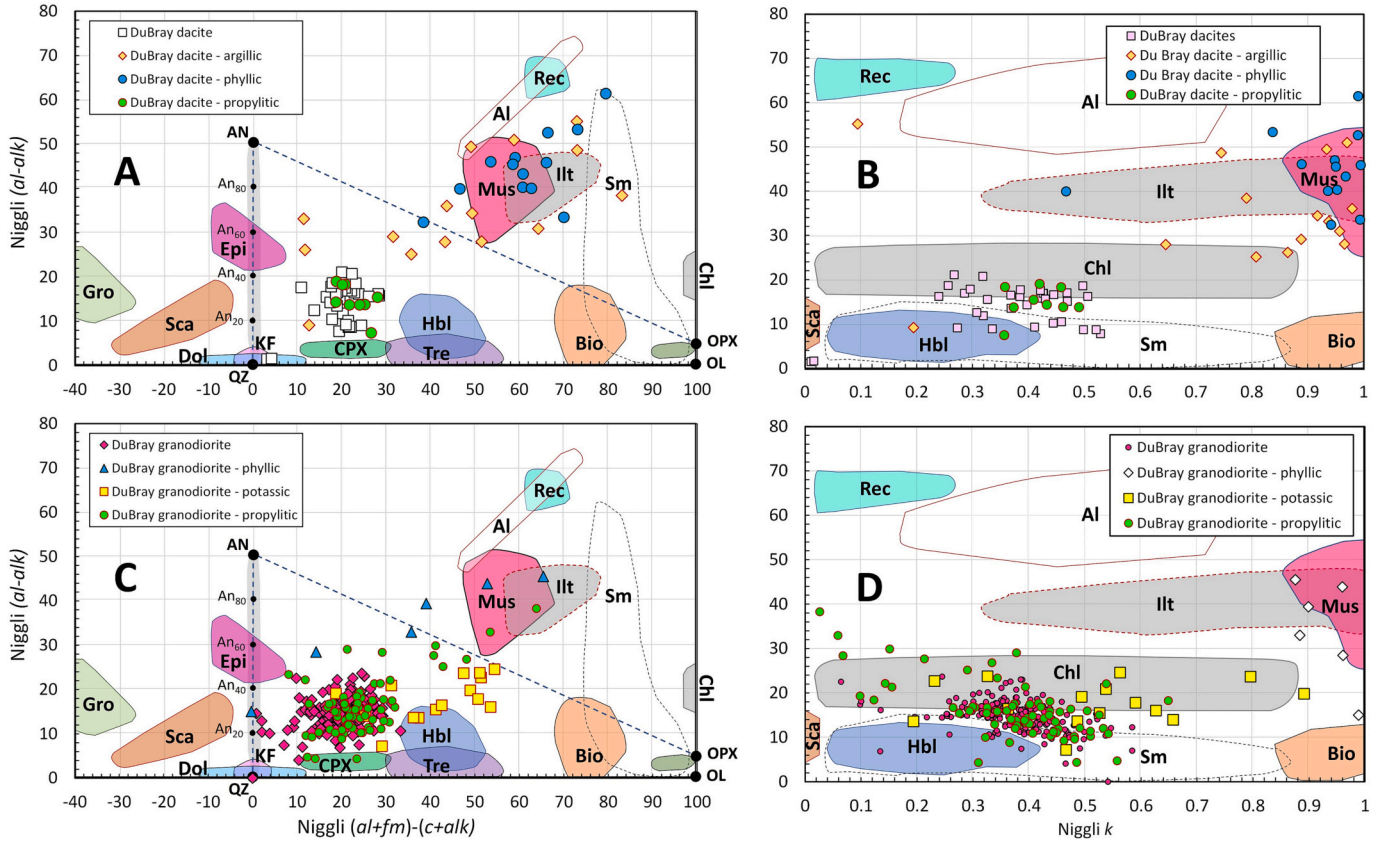

Fig. 18. Comparison of alteration in acid plutonic rocks from Nevada on Niggli (*al-alk*) versus (*al* + *fm*)-(*c* + *alk*) diagram (A) and the (*al-alk*) versus *k* diagrams. (A) and (B) dacites and altered dacites. (C) and (D) granodiorites and altered granodiorites. Data from du Bray et al. (2022). Abbreviations as in Fig. 1.

compared to the primary numbers, increasing or decreasing values of *si* (or derivative sums such as qz) for sandstones also serve as useful indicators for the maturity of the sediment.

This is illustrated using the chemostratigraphic dataset published by Ravidà et al. (2023) and based on samples from 4 wells drilled into Upper Permian and Lower Triassic sediments in southern Germany. Niggli (*al-alk*) versus *qz* and (*al-alk*) versus *c* plots for the Obernsees-1 well are shown in Fig. 19. The data trend in Fig. 19a from *qz* > 250 defines sandstones. The trend towards low *qz* and maximum (*al-alk*) defines siltstones and the trend towards (*al-alk*) = 0 and negative *qz* values defines most of the carbonate samples in the well. The values for *c* on Fig. 19b only go up to 45 and define a trend between clays and dolomite (c.f. Fig. 3). On both plots a small number of samples, all with very high *qz* values also have (*al-alk*) <0 and these values range as low as −15. These also tend to have the lowest *k* values in the whole dataset (0.55–0.7), reflecting an increased input from Na into the combined *alk* term. Values for the ratio of the molecular number for Na divided by *fm* in these samples are consistently >1.5 and therefore cannot arise from minerals like aegirine or riebeckite that have *Na/fm* around 0.5 and 0.2 respectively. The excess *alk* and lower *k* in these samples are most likely to reflect the presence of a pure Na mineral (e.g. halite) alongside K feldspar in some of these highly mature sandstones.

Niggli Numbers are plotted downhole for the Obernsees-1 well in Fig. 20. Major chemozones that were previously identified by Ravidà et al. (2023), primarily on the basis of trace element ratios and other mineral criteria, are designated CP2, CP3, CT1 and CT2. Boundaries between these major zones are shown by black dashed lines. Subzones within each chemozone (designated with the suffix a, b, c, etc) are separated by blue dashed lines (Fig. 20). For simplicity, the Niggli data are presented as a whole and no attempt has been made to classify and subdivide them into sandstone, siltstone or carbonate categories. Grain size effects can be seen, particularly in zones CT1 and CT2, on the *qz* and *ti* profiles where the data separate into populations with high and low values. Siltstones have low *qz* and high *ti*, whereas sandstones show the opposite. Even acknowledging this simplification, it is clear that the Niggli trends for Obernsees-1 presented in Fig. 20 show demonstrable breaks and/or trend inflections for at least one parameter (and more commonly multiple parameters) that coincide with all of the boundaries defined by Ravidà et al. (2023) between the major chemozones and also with their associated subzones. Furthermore, based on an offset in *k* and (*si x (al-alk)/c*) and inflections in the trends for *si, ti, mg* and (*al-alk*)/*c* the Niggli profiles suggest evidence for two further internals subdivisions, at -1070 m in subzone CT1b and at -1185 m in subzone CT1a (Fig. 20).

It is equally important to demonstrate whether the Niggli profiles remain clear and robust enough to still be recognizable in other wells through the same sequence. This is tested in Fig. 21 where correlations for Obernsees-1 and the Lindau-1 well drilled ~20 km to the northeast are compared. Niggli profiles for ti, qz and *mg* in each well show strong similarities in terms of data trends and direction(s), inflection points and magnitude for the upper CP2, CP3b, CP3c, CT1a and lower CT1b chemostratigraphic zones and subzones defined and correlated by Ravidà et al. (2023). But there are also differences, most notably the strong enrichment in *ti* and *mg* that is observed in subzone CP3a in the Obernsees-1 well (Fig. 20) is not evident for CP3a the Lindau-1 well. Despite this, the degree to which the Niggli profiles retain similarities and can be reliably correlated between the two sequences is clear and demonstrates the potential usefulness of the numbers for chemostratigraphy.

While they are largely based on major elements and cannot provide the same detailed information about provenance or tectonic environment that comes from trace element ratios (e.g. Ramkumar et al., 2021),

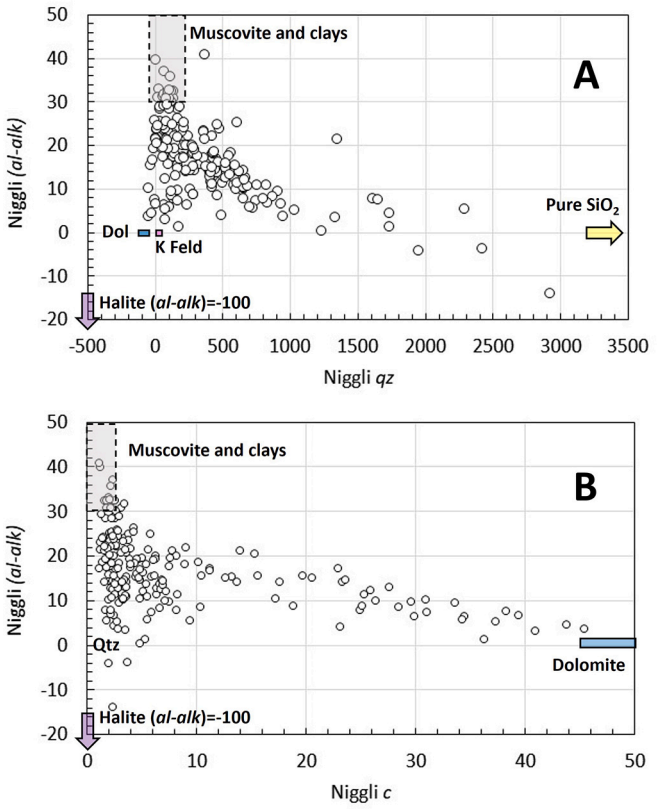

Fig. 19. (A) Niggli (*al-alk*) versus *qz*; and (B) Niggli (*al-alk*) versus c for samples from the Obernsees-1 well. Data from Ravidà et al. (2023). Fields for quartz (Qtz), K feldspar, dolomite and muscovite and clays are indicated. Halite plots off scale at (*al-alk*) = −100 in both cases.

the Niggli profiles nevertheless provide useful additional information about maturity of sandstones (*qz*), relative proportions of carbonate to clay ((*al-alk*)/*c*) and type(s) of carbonate in the sequence (*c* values and *mg*). They should be most fairly viewed as a complimentary tool to immobile trace element ratios, both to aid interpretation and give additional confidence when establishing major chemzones and subzones in a sedimentary sequence. Niggli calculations are rapid compared to Principle Component or Regression analysis and should be relatively straightforward to incorporate to existing chemostratigraphy workflows, such as those described by Craigie (2018).

4. Conclusions

The previous sections have introduced Niggli Numbers and the key relationships between minerals that can be represented on binary plots or using profiles. This view of how to link bulk chemistry with mineralogy is well suited to applications in modern petrology and particularly to geochemistry applied to exploration for minerals or hydrocarbons. Niggli Numbers provide a rapid and simple means of addressing the well-known problem of closure that is independent of, but also complimentary to, the element ratio approaches previously discussed. Vastly improved availability of data, digital computing and automated plotting software overcome all of the great handicaps faced by Niggli, his coworkers and the generation who came immediately after him, when all numbers had to be calculated and plotted by hand, and were partially representative of rock suites at best.

The design of the Niggli calculation has in-built simplicity and flexibility with respect to rock type, availability or non-availability of silica data, oxidation state of iron or volatile content. The composition of any rock or mineral that (at a minimum) contains some or all of the elements needed for the 4 primary numbers can be expressed as Niggli Numbers and the case studies presented above have demonstrated applications for igneous, metamorphic and sedimentary rocks using this single scheme. As discussed in Section 2, numbers exist within a consistent and logical framework, are results often intuitive (e.g. ⟨1,1,⟩1, 50, 100, etc) and straightforward to interpret, especially when unknown data are

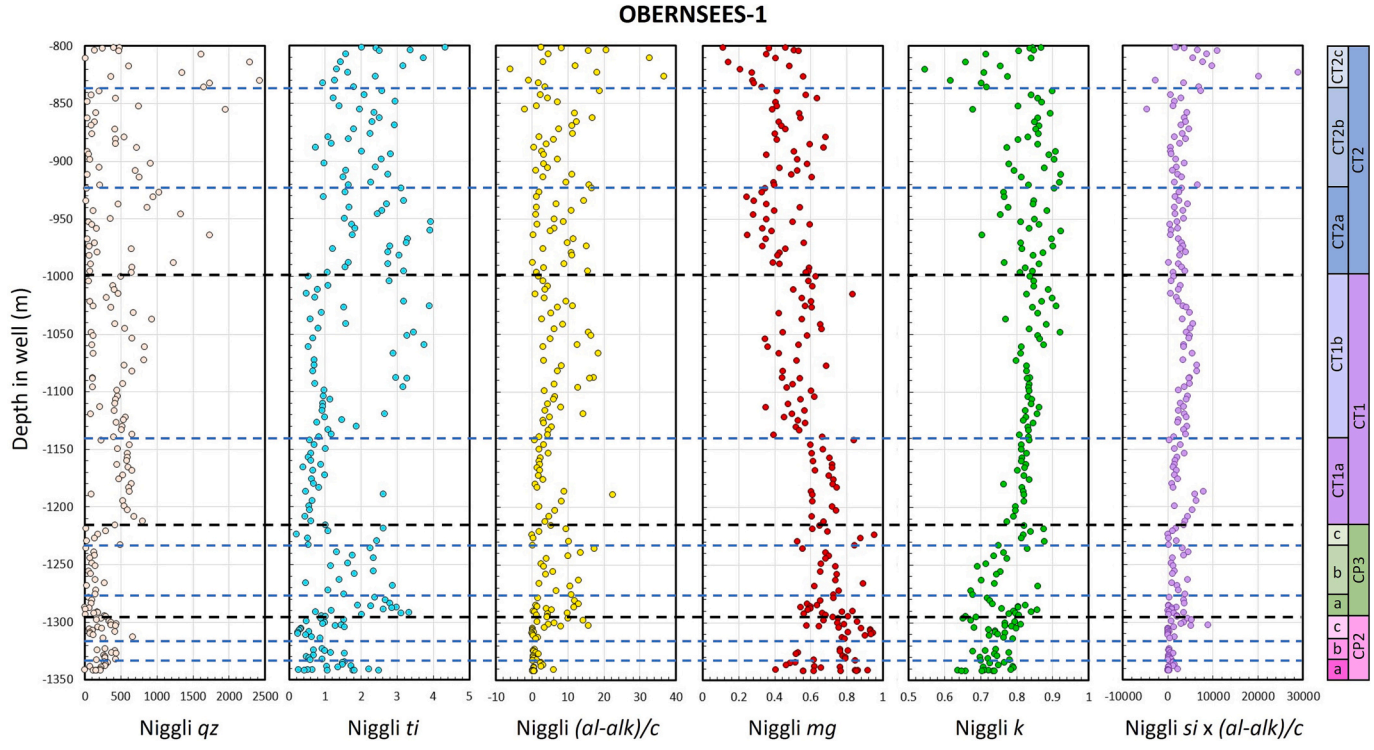

Fig. 20. Downhole Niggli Number profiles for the Obernsees-1 well compared to the chemostratigraphic interpretation presented by Ravidà et al. (2023).

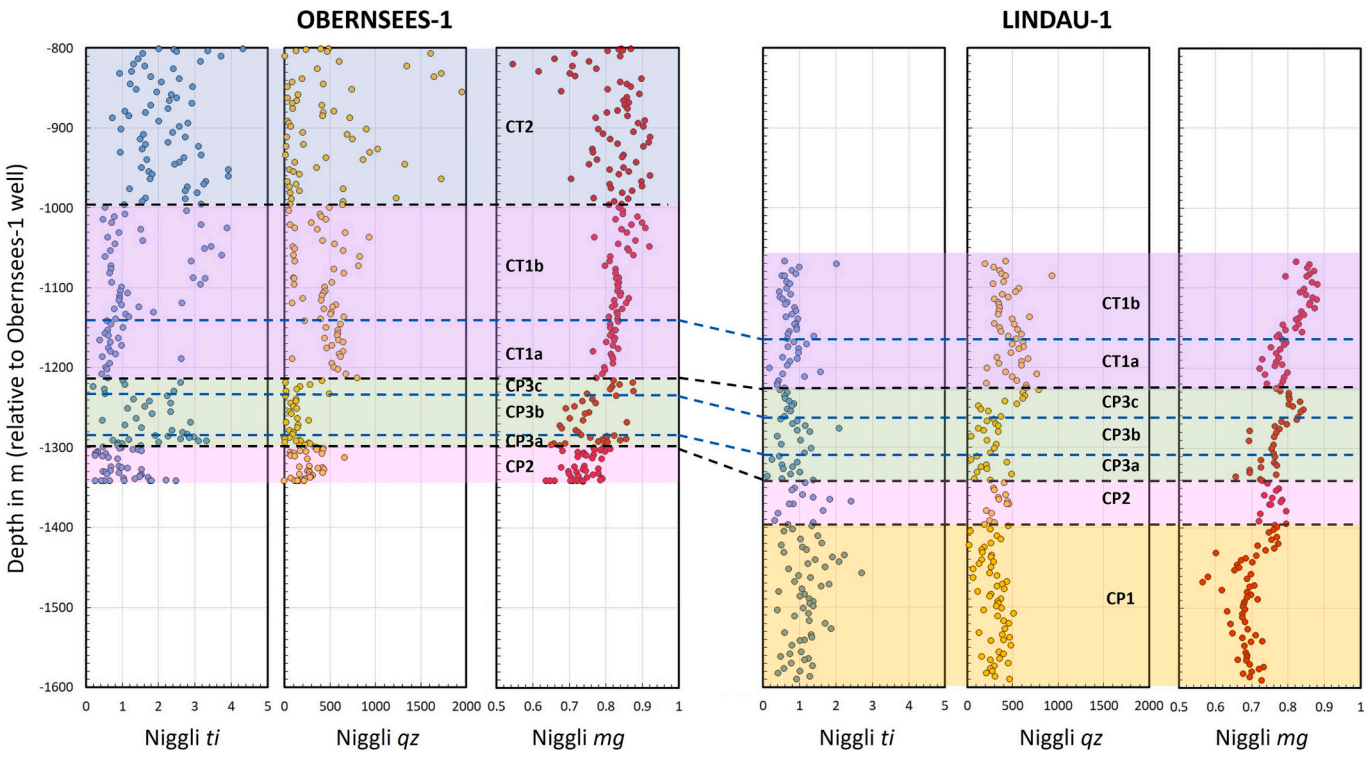

Fig. 21. Downhole Niggli profiles for *ti*, *qz* and *mg* compared between the Obernsees-1 and Lindau-1 wells and against the chemostratigraphic interpretation by Ravidà et al. (2023). Depths for the Lindau-1 well are corrected on to the same depth scale as used for the Obernsees-1 well.

compared to pre-established mineral fields in Niggli space. This is often easier to visualize than would be possible on Harker plots or other binary diagrams where differentiation may produce large variations (e.g. in Si, Mg, Fe, Ca, etc) in a single mineral, and is particularly useful when attempting to represent and appreciate how whole rock data reflect mineralogical changes with stratigraphy (see Sections 3.1 and 3.4).

Niggli Numbers are primarily based on major elements and will not be as useful as trace elements or isotopes for fingerprinting key factors such as tectonic settings or mantle domains or contamination by crust of a particular age. But, as explained above, Niggli Numbers have many useful applications alongside these other data in fields such as studies of alteration mineralogy or chemostratigraphy, that often came into existence or only became fully developed after the Niggli method fell out of fashion. It is a great shame that the flexibility and potential of Niggli Numbers has been largely forgotten, even where it offers an alternative mitigation of the closure problem. This study has demonstrated a number of these applications, and there are likely to be many more to be found if people are willing to experiment with the numbers and apply them to larger and even more diverse datasets than have been illustrated here. The calculation scheme and the plots and associated mineral fields presented here are readily coded and it should be straightforward to incorporate them as additional functionality in modern geochemical software packages such as ioGas®, alongside the elemental ratio tools and other normalization and discrimination diagrams that already exist (e.g. Stanley, 2020). Furthermore, because each number or sum or ratio may carry an enormous amount of useful petrological information, binary diagrams or the variations and inflections in downhole number profiles should be valuable inputs for machine-learning applications designed to predict lithologies or detect boundaries between lithologies using geochemical data alone, or using geochemistry in combination with spectroscopic methods (e.g. Acosta et al., 2020; He et al., 2022).

Niggli Numbers represent elegant technology from the early 20th century that was by its very nature simple and flexible enough to accommodate the computational limitations of the period. That approach to reducing complexity and the framework it employs, provide useful solutions for interpreting geochemical data in relation to mineralogy that are different but complimentary to many modern methods. Niggli Numbers are analogous to an old tool that has laid forgotten and rusting in the bottom of a tool box for many decades. The tool still works and if it is cleaned and made new again, there may be a myriad of new uses that it can be put to. Hopefully this article will encourage the global geochemical community to re-evaluate Niggli Numbers and discover additional applications for them beyond those presented here.

CRediT authorship contribution statement

Iain McDonald: Conceptualization, Data curation, Formal analysis, Funding acquisition, Investigation, Methodology, Project administration, Resources, Software, Supervision, Validation, Visualization, Writing – original draft, Writing – review & editing.

Declaration of Competing Interest

The authors declare the following financial interests/personal relationships which may be considered as potential competing interests:

Iain McDonald reports financial support was provided by Natural Environment Research Council. Iain McDonald reports financial support was provided by Anglo American.

Data availability

No new data were generated during this work. Sources for data used in this research are presented in Table 1.

Acknowledgements

This paper would not have been possible without Paul Niggli's visionary work and the relevance and value of Niggli Numbers being preserved and taught over the last 50 years by a small number of dedicated and far-sighted geochemists. Foremost among this group is

Professor Bernard E. Leake who introduced the Niggli scheme to me, along with many other final year undergraduate students, at the University of Glasgow. I am truly grateful to Bernard for his encouragement to pursue this reimagining and for providing his copies of Niggli's books so that I could understand and explore the principles behind the scheme first hand. I am thankful to Jon Blundy and an anonymous reviewer for very helpful comments and advice that brought the paper to its final form, and to Marco Fiorentini for his editorial support. Elements of this work were supported by the Natural Environment Research Council under project NE/P017312/1 (From arc magmas to ores (FAMOS): a mineral systems approach) and by Anglo American through the "Northern Limb NL4D" consortium project.

Appendix A. Supplementary data

Supplementary data to this article can be found online at https://doi.org/10.1016/j.chemgeo.2023.121915.

References

Abdel-Karim, A.A., Puskás, Z., Jánosi, M., 2002. Origin and tectonic history of some metamorphic rocks from southern Sinai, Egypt. Acta Mineralogica-Petrographica 43, 27–38.
Acosta, I.C.C., Khodadadzadeh, M., Tolosana-Delgado, R., Gloaguen, R., 2020. Drill-core hyperspectral and geochemical data integration in a superpixel-based machine learning framework. IEEE J. Selected Topics Appl Earth Observ. Remote Sens. 13, 4214–4228.
Afshooni, S.Z., Mirnejad, H., Esmaeily, D., Haroni, H.A., 2013. Mineral chemistry of hydrothermal biotite from the Kahang porphyry copper deposit (NE Isfahan), Central Province of Iran. Ore Geol. Rev. 54, 214–232.
Aitchison, J., 1982. The statistical analysis of compositional data. J. Roy. Stat. Soc. B 44, 139–177.
Antao, S.M., 2021. Crystal chemistry of six grossular garnet samples from different well-known localities. Minerals 11, 767.
Armitage, P.E.B., McDonald, I., Edwards, S.J., Manby, G.M., 2002. Platinum-group element mineralization in the Platreef and calc-silicate footwall at Sandsloot, Potgietersrus District, South Africa. Appl. Earth Sci. 111, 36–45.
Ashwal, L.D., Webb, S.J., Knoper, M.W., 2005. Magmatic stratigraphy in the Bushveld Northern Lobe: continuous geophysical and mineralogical data from the 2950m Bellevue drillcore. S. Afr. J. Geol. 108, 199–232.
Barros, R., Kaeter, D., Menuge, J.F., Škoda, R., 2020. Controls on chemical evolution and rare element enrichment in crystallising albite-spodumene pegmatite and wallrocks: constraints from mineral chemistry. Lithos 352, 105289.
Buccianti, A., Grunsky, E., 2014. Compositional data analysis in geochemistry: are we sure to see what really occurs during natural processes? J. Geochem. Explor. 141, 1–5.
Buchanan, D.L., Nolan, J., Suddaby, P., Rouse, J.E., Viljoen, M.J., Davenport, J.W.J., 1981. The genesis of sulfide mineralization in a portion of the Potgietersrus limb of the Bushveld Complex. Econ. Geol. 76, 568–579.
Burri, C., Niggli, P., 1945. Die jungen Eruptivgesteine des mediterranen Orogens: Die Ophiolithe-Allgemeines über das Verhalten basischer Magmen-Berechnungsmethoden. Erster hauptteil. Kommissionsverlag von Guggenbühl & Huber, Schweizer Spiegel Verlag.
Burri, C., Niggli, P., 1949. Die jungen Eruptivgesteine des mediterranen Orogens: Der Chemismus der postophiolitischen Eruptivgesteine. Zweiter Hauptteil. Kommissionsverlag von Guggenbühl & Huber, Schweizer Spiegel Verlag.
Butler, J.C., 1981. Effect of various transformations on the analysis of percentage data. Math. Geol. 13, 53–68.
Cawthorn, R.G., 1996. Re-evaluation of magma compositions and processes in the uppermost Critical Zone of the Bushveld Complex. Mineral. Mag. 60, 131–148.
Cawthorn, R.G., Barton, J.M., Vilijoen, M.J., 1985. Interaction of floor rocks with the Platreef on Overysel, Potgietersrus, Northern Transvaal. Econ. Geol. 80, 988–1006.
Chayes, F., 1960. On correlation between variables of constant sum. J. Geophys. Res. 65, 4185–4193.
Chayes, F., 1968. Identity of Expected Interdependence Between Pairs of Niggli Numbers and Pairs of Analogous Remaining Space Variables, Vol. 1967-68. Carnegie Institute of Washington Yearbook, p. 235, 67.
Coats, R.R., 1952. Magmatic differentiation in Tertiary and Quaternary volcanic rocks from Adak and Kanaga islands, Aleutian Islands, Alaska. Geol. Soc. Am. Bull. 63, 485–514.
Craigie, N., 2018. Principles of elemental chemostratigraphy. Advances in Oil and Gas Exploration & Production, Rudy Swennen. Pract. User Guide. https://doi.org/10.1007/978-3-319-71216-1 p189.
Craigie, N.W., Rees, A., MacPherson, K., Berman, S., 2016. Chemostratigraphy of the Ordovician Sarah Formation, North West Saudi Arabia: an integrated approach to reservoir correlation. Mar. Pet. Geol. 77, 1056–1080.
Cross, W., Iddings, J.P., Pirsson, L.V., Washington, H.S., 1903. Quantitative Classification of Igneous Rocks. University of Chicago Press.
Cullers, R.L., 2000. The geochemistry of shales, siltstones and sandstones of Pennsylvanian–Permian age, Colorado, USA: implications for provenance and metamorphic studies. Lithos 51, 181–203.
de Klerk, W.J., 1991. Petrogenesis of the Upper Critical Zone in the Western Bushveld Complex with Emphasis on the UG1 Footwall and Bastard Units. Unpublished Ph.D. thesis,. Rhodes University, 424pp.
Dessimoz, M., Müntener, O., Ulmer, P., 2012. A case for hornblende dominated fractionation of arc magmas: the Chelan Complex (Washington Cascades). Contrib. Mineral. Petrol. 163, 567–589.
DIGIS Team, 2023a. 2023–06-2JETOA_ANDESITE_part1.csv. In: GEOROC Compilation: Rock Types. https://doi.org/10.25625/2JETOA/GGEYNT. GRO.data, V7.
DIGIS Team, 2023b. 2023-06-SGFTFN_AMPHIBOLES.csv. In: GEOROC Compilation: Minerals. https://doi.org/10.25625/SGFTFN/NYH52V (GRO.data, V7).
DIGIS Team, 2023c. 2023–06-2JETOA_BASALT_part1.csv. In: GEOROC Compilation: Rock Types. https://doi.org/10.25625/2JETOA/FK8F4K. GRO.data, V7.
DIGIS Team, 2023d. 2023-06-SGFTFN_CARBONATES.csv. In: GEOROC Compilation: Minerals. https://doi.org/10.25625/SGFTFN/HMF8JI (GRO.data, V7).
DIGIS Team, 2023e. 2023–06-2JETOA_DACITE_part1.csv. In: GEOROC Compilation: Rock Types. https://doi.org/10.25625/2JETOA/1CJK9P. GRO.data, V7.
DIGIS Team, 2023f. 2023-06-SGFTFN_CLAY_MINERALS.csv. In: GEOROC Compilation: Minerals. https://doi.org/10.25625/SGFTFN/WYFBAO (GRO.data, V7).
DIGIS Team, 2023g. 2023–06-2JETOA_RHYOLITE_part1.csv. In: GEOROC Compilation: Rock Types. https://doi.org/10.25625/2JETOA/J5PXUP. GRO.data, V7.
DIGIS Team, 2023h. 2023-06-SGFTFN_CLINOPYROXENES.csv. In: GEOROC Compilation: Minerals. https://doi.org/10.25625/SGFTFN/KXSFXD (GRO.data, V7).
DIGIS Team, 2023i. 2023-06-SGFTFN_FELDSPARS.csv. In: GEOROC Compilation: Minerals. https://doi.org/10.25625/SGFTFN/MD8FPK (GRO.data, V7).
DIGIS Team, 2023j. 2023-06-SGFTFN_GARNETS.csv. In: GEOROC Compilation: Minerals. https://doi.org/10.25625/SGFTFN/QN2T7X (GRO.data, V7).
DIGIS Team, 2023k. 2023-06-SGFTFN_MICA.csv. In: GEOROC Compilation: Minerals. https://doi.org/10.25625/SGFTFN/LNCUGZ (GRO.data, V7).
DIGIS Team, 2023l. 2023-06-SGFTFN_OLIVINES.csv. In: GEOROC Compilation: Minerals. https://doi.org/10.25625/SGFTFN/LUPQOB (GRO.data, V7).
DIGIS Team, 2023m. "2023-12-SGFTFN_SPINELS.csv", GEOROC Compilation: Minerals. https://doi.org/10.25625/SGFTFN/RJSWBH,. GRO.data, V9.
DIGIS Team, 2023n. "2023-12-SGFTFN_TITANITES.csv", GEOROC Compilation: Minerals. https://doi.org/10.25625/SGFTFN/VOWPTI. GRO.data, V9.
DIGIS Team, 2023o. "2023-12-2JETOA_CARBONATITE.csv", GEOROC Compilation: Rock Types. https://doi.org/10.25625/2JETOA/ZFNZST. GRO.data, V9.
DIGIS Team, 2023p. "2023-12-2JETOA_KIMBERLITE.csv", GEOROC Compilation: Rock Types. https://doi.org/10.25625/2JETOA/GAUL1W. GRO.data, V9.
DIGIS Team, 2023q. "2023-12-2JETOA_NEPHELINITE.csv", GEOROC Compilation: Rock Types. https://doi.org/10.25625/2JETOA/4X485M. GRO.data, V9.
DIGIS Team, 2023r. "2023-12-2JETOA_GABBRO.csv", GEOROC Compilation: Rock Types. https://doi.org/10.25625/2JETOA/NWDHEP. GRO.data, V9.
Du Bray, E.A., Ressel, M.W., Barnes, C.G., 2007. Geochemical database for intrusive rocks of North-Central and Northeast Nevada. U.S. Geol. Surv. Data Ser. 244, 1–62.
du Bray, Edward A., Ressel, Michael W., Barnes, Calvin G., 2022. Geochemical Data for Intrusive Rocks of North-Central and Northeast Nevada. https://doi.org/10.25625/MTS04.
Evans, B.W., Leake, B.E., 1960. The composition and origin of the striped amphibolites of Connemara, Ireland. J. Petrol. 1, 337–363.
Franchi, F., 2018. Petrographic and geochemical characterization of the lower Transvaal Supergroup stromatolitic dolostones (Kanye Basin, Botswana). Precambrian Res. 310, 93–113.
Frimmel, H.E., Tack, L., Basei, M.S., Nutman, A.P., Boven, A., 2006. Provenance and chemostratigraphy of the Neoproterozoïc West Congolian Group in the Democratic Republic of Congo. J. Afr. Earth Sci. 46, 221–239.
Grobler, D.F., Brits, J.A.N., Maier, W.D., Crossingham, A., 2019. Litho-and chemostratigraphy of the Flatreef PGE deposit, northern Bushveld Complex. Mineral. Deposita 54, 3–28.
Gros, K., Słaby, E., Birski, Ł., Kozub-Budzyń, G., Sláma, J., 2020. Geochemical evolution of a composite pluton: insight from major and trace element chemistry of titanite. Mineral. Petrol. 114, 375–401.
Harris, C., Chaumba, J.B., 2001. Crustal contamination and fluid-rock interaction during the formation of the Platreef, Northern Limb of the Bushveld Complex, South Africa. J. Petrol. 42, 1321–1347.
He, Y., Zhou, Y., Wen, T., Zhang, S., Huang, F., Zou, X., Ma, X., Zhu, Y., 2022. A review of machine learning in geochemistry and cosmochemistry: Method improvements and applications. Appl. Geochem. 140, 105273.
Holwell, D.A., 2006. The Roles of Magmatism, Contamination and Hydrothermal Processes in the Development of Platreef Mineralisation, Bushveld Complex, South Africa. Unpublished PhD thesis,. Cardiff University, 285pp.
Holwell, D.A., Boyce, A.J., McDonald, I., 2007. Sulfur isotope variations within the Platreef Ni-Cu-PGE deposit: Genetic implications for the origin of sulfide mineralization. Econ. Geol. 102, 1091–1110.
Holwell, D.A., McDonald, I., 2006. Petrology, geochemistry and the mechanisms determining the distribution of platinum-group element and base metal sulphide mineralisation in the Platreef at Overysel, northern Bushveld Complex, South Africa. Mineralium Deposita 41, 575–598.
Hulbert, L.J., 1983. A Petrographical Investigation of the Rustenburg Layered Suite and Associated Mineralisation South of Potgietersrus. Unpublished DSc dissertation,. University of Pretoria, 511 p.
Huthmann, F.H., Yudovskaya, M.A., Kinnaird, J., McCreesh, M., McDonald, I., 2018. Geochemistry and PGE of the lower mineralised Zone of the Waterberg Project, South Africa. Ore Geol. Rev. 92, 161–185.

Ihlenfeld, C., Keays, R.R., 2011. Crustal contamination and PGE mineralisation in the Platreef, Bushveld complex, South Africa: evidence for multiple contamination events and transport of magmatic sulphides. Mineral. Deposita 46, 813–832.
Ishikawa, Y., Sawaguchi, T., Iwaya, S., Horiuchi, M., 1976. Delineation of prospecting targets for Kuroko deposits based on modes of volcanism of underlying dacite and alteration haloes. Min. Geol. 26, 105–117.
Johannsen, A., 1931. A Descriptive Petrology of the Igneous Rocks. Volume 1, Introduction, Textures, Classifications and Glossary. University of Chicago Press, 267pp.
Keir-Sage, E., Leybourne, M.I., Jugo, P.J., Grobler, D.F., Mayer, C.C., 2021. Assessing the extent of local crust assimilation within the Flatreef, northern limb of the Bushveld Igneous Complex, using sulfur isotopes and trace element geochemistry. Mineral. Deposita 56, 91–102.
Kennedy, B., 2019. Unconventional Olivine-Rich Cumulates, Magma Dynamics and Development of Platinum-Group Element Mineralisation in the Main Zone of the Northern Bushveld Complex. Unpublished PhD thesis,. Cardiff University, 457pp.
Kim, J.D., Moon, H.S., Jin, S.J., Kim, I.J., 1992. Mineral chemistry and stable isotope composition of sericite from the Sangdong sericite mine in the Kimhae area. Econ. Environ. Geol. 25 (3), 275–282.
Kinnaird, J.A., 2005. Geochemical evidence for multiphase emplacement in the southern Platreef. Appl. Earth Sci. 114, 225–242.
Kinnaird, J.A., McDonald, I., 2018. The northern limb of the Bushveld Complex: a new economic frontier. Soc. Econ. Geol. Spec. Publ. 21, 157–176.
Kinnaird, J.A., Yudovskaya, M., McCreesh, M., Huthmann, F., Botha, T.J., 2017. The Waterberg platinum group element deposit: atypical mineralization in mafic-ultramafic rocks of the Bushveld Complex, South Africa. Econ. Geol. 112, 1367–1394.
Kruger, F.J., 2005. Filling the Bushveld Complex magma chamber: lateral expansion, roof and floor interaction, magmatic unconformities, and the formation of giant chromitite, PGE and Ti-V-magnetitite deposits. Mineralium Deposita 40, 451–472.
Large, R.R., Gemmell, J.B., Paulick, H., Huston, D.L., 2001. The alteration box plot: A simple approach to understanding the relationship between alteration mineralogy and lithogeochemistry associated with volcanic-hosted massive sulfide deposits. Econ. Geol. 96, 957–971.
Le Maitre, R.W., Bateman, P., Dudek, A., Keller, J., Lameyre Le Bas, M.J., Sabine, P.A., Schmid, R., Sorensen, H., Streckheisen, A., Woolley, A.R., Zanettin, B., 1989. A Classification of Igneous Rocks and a Glossary of Terms. Blackwell, Oxford.
Leake, B.E., 1964. The chemical distinction between Ortho- and Para-amphibolites. J. Petrol. 5, 238–254.
Leake, B.E., Singh, D., 1986. The Delaney Dome Formation, Connemara, W. Ireland, and the geochemical distinction of ortho-and para-quartzofeldspathic rocks. Mineral. Mag. 50, 205–215.
Leake, B.E., Skirrow, G., 1960. The pelitic hornfelses of the Cashel-Lough Wheelaun intrusion, county Galway, Eire. J. Geol. 68, 23–40.
Lundgaard, K.L., Tegner, C., Cawthorn, R.G., Kruger, F.J., Wilson, J.R., 2006. Trapped intercumulus liquid in the Main Zone of the eastern Bushveld Complex, South Africa. Contrib. Mineral. Petrol. 151, 352–369.
Maier, W.D., De Klerk, L., Blaine, J., Manyeruke, T., Barnes, S.-J., Stevens, M.V.A., Mavrogenes, J.A., 2008. Petrogenesis of contact-style PGE mineralisation in the northern lobe of the Bushveld Complex: comparison of data from the farms Rooipoort, Townlands, Drenthe and Nonnenwerth. Mineral. Deposita 43, 255–280.
Manyeruke, T.D., Maier, W.D., Barnes, S.J., 2005. Major and trace element geochemistry of the Platreef on the farm Townlands, northern Bushveld Complex. South African J. Geol. 108, 381–396.
Mathieu, L., 2018. Quantifying hydrothermal alteration: A review of methods. Geosciences 8, 245.
Mavrogonatos, C., Voudouris, P., Spry, P.G., Melfos, V., Klemme, S., Berndt, J., Baker, T., Moritz, R., Bissig, T., Monecke, T., Zaccarini, F., 2018. Mineralogical study of the advanced argillic alteration zone at the Konos Hill Mo–Cu–Re–Au porphyry prospect, NE Greece. Minerals 8, 479.
McCreesh, M.J.G., 2016. An Investigation of the Mineralisation in the Waterberg PGE Deposit, South Africa. Unpublished MSc thesis,. University of the Witwatersrand, 226pp.
McDonald, I., Holwell, D.A., 2011. Geology of the Northern Bushveld Complex and the setting and genesis of the Platreef Ni-Cu-PGE deposit. In: Ripley, E., Li, C. (Eds.), Magmatic Ni-Cu and PGE Deposits: Geology, Geochemistry and Genesis: Reviews in Economic Geology, Vol. 17. Society of Economic Geologists, pp. 297–328.
McDonald, I., Holwell, D.A., Armitage, P.E.B., 2005. Geochemistry and mineralogy of the Platreef and "Critical Zone" cumulates of the Northern limb of the Bushveld Complex, South Africa: implications for Bushveld stratigraphy and the development of PGE mineralisation. Mineral. Deposita 40, 526–549.
McDonald, I., Holwell, D.A., Wesley, B., 2009. Assessing the potential involvement of an early magma staging chamber in the generation of the Platreef Ni-Cu-PGE deposit in the northern limb of the Bushveld Complex: a pilot study of the Lower Zone Complex at Zwartfontein. Appl. Earth Sci. 118, 5–20.
Mercier-Langevin, P., 2000. Les minéralisations aurifères au sein de la tonalite de La Grande-Sud. Baie-James, Québec. Université du Québec à Chicoutimi.
Mitchell, A.A., Manthree, R., 2002. The Giant Mottled Anorthosite: a transitional sequence at the top of the Upper Critical Zone of the Bushveld Complex. S. Afr. J. Geol. 105, 15–24.
Miyano, T., Beukes, N.J., 1984. Phase relations of stilpnomelane, ferri-annite, and riebeckite in very low-grade metamorphosed iron-formations. S. Afr. J. Geol. 87, 111–124.
Miyano, T., Beukes, N.J., 1997. Mineralogy and petrology of the contact metamorphosed amphibole asbestos-bearing Penge iron formation, Eastern Transvaal, South Africa. J. Petrol. 38 (5), 651–676.
Muthuswami, T.N., 1952. Niggli's principles of Igneous petrogenesis. In: Proceedings of the Indian Academy of Sciences, Section A, Vol. 36. Indian Academy of Sciences, pp. 1–40. No. 1.
Nex, P.A., 2005. The structural setting of mineralisation on Tweefontein Hill, northern limb of the Bushveld Complex, South Africa. Appl. Earth Sci. 114, 243–251.
Nex, P.A.M., Cawthorn, R.G., Kinnaird, J.A., 2002. Geochemical effects of magma addition: compositional reversals and decoupling of trends in the Main Zone of the western Bushveld Complex. Mineral. Mag. 66, 833–856.
Nicholls, J., Gordon, T.M., 1994. Procedures for the calculation of axial ratios on Pearce element-ratio diagrams. Can. Mineral. 32, 969–977.
Niggli, P., 1920. Lehrbuch der Mineralogie. Verlag, Gebruder Borntraeger, Berlin, 467pp.
Niggli, P., 1952. The chemistry of the Keweenawan lavas. Bowen 2, 381.
Niggli, P., 1954. Rocks and Mineral Deposits. W.H. Freeman and Co, San Francisco, 559pp.
Niggli, P., Winterhalter, R.U., Quervain, F.D., 1930. Chemismus schweizerischer Gesteine. Beit. Geol. Schweiz, Geotech. Ser. v 14.
Nodder, S.M., 2015. Correlating the Bushveld's northern limb with the eastern and western limbs: a geochemical and petrological study. MESci Dissertation. Cardiff University, 257pp.
Panigrahi, M.K., Naik, R.K., Pandit, D., Misra, K.C., 2008. Reconstructing physico-chemical parameters of hydrothermal mineralization of copper at the Malanjkhand deposit, India, from mineral chemistry of biotite, chlorite and epidote. Geochem. J. 42, 443–460.
Parry, W.T., Ballantyne, J.M., Jacobs, D.C., 1984. Geochemistry of hydrothermal sericite from Roosevelt Hot Springs and the Tintic and Santa Rita porphyry copper systems. Econ. Geol. 79 (1), 72–86.
Parsapoor, A., Khalili, M., Tepley, F., Maghami, M., 2015. Mineral chemistry and isotopic composition of magmatic, re-equilibrated and hydrothermal biotites from Darreh-Zar porphyry copper deposit, Kerman (Southeast of Iran). Ore Geol. Rev. 66, 200–218.
Pearce, T.H., 1968. A contribution to the theory of variation diagrams. Contrib. Mineral. Petrol. 19, 142–157.
Pearce, T.J., Besly, B.M., Wray, D.S., Wright, D.K., 1999. Chemostratigraphy: a method to improve interwell correlation in barren sequences—a case study using onshore Duckmantian/Stephanian sequences (West Midlands, UK). Sediment. Geol. 124, 197–220.
Pearce, T.J., Wray, D.S., Ratcliffe, K.T., Wright, D.K., Moscariello, A., Collinson, J.D., Evans, D.J., Holliday, D.W., Jones, N.S., 2005. Chemostratigraphy of the upper carboniferous schooner formation, southern North Sea. Carboniferous hydrocarbon geology: the southern North Sea and surrounding onshore areas. Yorkshire Geological Society, Occasional Publications series 7, 147–164.
Ramkumar, M., Nagarajan, R., Santosh, M., 2021. Advances in sediment geochemistry and chemostratigraphy for reservoir characterization. Energy Geosci. 2, 308–326.
Ravidà, D.C., Caracciolo, L., Heins, W.A., Stollhofen, H., 2023. Towards an improved discrimination and correlation of Permian-lower Triassic sediments in Central Europe: a chemostratigraphic approach. Sediment. Geol. 452 p.106408.
Rehkopff, A., 1984. Origin of quartzo-feldspathic supracrustal rocks from the central part of the Nagssugtoqidian mobile belt of West Greenland. Rapp. Grønl. Geol. Unders. 117, 1–26.
Roelofse, F., Ashwal, L.D., 2012. The Lower Main Zone in the Northern Limb of the Bushveld Complex: a 1·3 km thick sequenceof intruded and variably contaminated crystal mushes. J. Petrol. 53, 1449–1476.
Runyon, S.E., Seedorff, E., Barton, M.D., Steele-MacInnis, M., Lecumberri-Sanchez, P., Mazdab, F.K., 2019. Coarse muscovite veins and alteration in porphyry systems. Ore Geol. Rev. 113, 103045.
Seabrook, C.L., 2005. The Upper Critical and Lower Main Zones of the Eastern Bushveld Complex. Unpublished PhD Thesis,. University of the Witwatersrand, 284pp.
Seedorff, E., Dilles, J.H., Proffett, J.M., Einaudi, M.T., Zurcher, L., Stavast, W.J., Johnson, D.A., Barton, M.D., 2005. Porphyry Deposits: Characteristics and Origin of Hypogene Features.
Senior, A., Leake, B.E., 1978. Regional metasomatism and the geochemistry of the Dalradian metasediments of Connemara, western Ireland. J. Petrol. 19, 585–625.
Setera, J.B., VanTongeren, J.A., 2018. Lateral variability in the Upper Main Zone, Bushveld Complex, owing to directional magma recharge and emplacement from north to south. J. Petrol. 59, 1763–1786.
Smith, J.W., 2014. The Nature and Origin of PGE Mineralisation in the Rooipoort Area, Northern Bushveld Complex, South Africa. Unpublished PhD Thesis,. University of Leicester, 291pp.
South African Committee for Stratigraphy, 1980. Stratigraphy of South Africa, Part 1 (Compiler, L.E. Kent). Geological Survey of South Africa Handbook 8. Geological Survey of South Africa, Pretoria, 690pp.
Środoń, J., Morgan, D.J., Eslinger, E.V., Eberl, D.D., Karlinger, M.R., 1986. Chemistry of illite/smectite and end-member illite. Clay Clay Miner. 34, 368–378.
Stanley, C., 2017. Lithogeochemical classification of igneous rocks using Streckeisen ternary diagrams. Geochem. Explor. Environ. Anal. 17, 63–91.
Stanley, C.R., 2020. Molar element ratio analysis of lithogeochemical data: a toolbox for use in mineral exploration and mining. Geochem. Explor. Environ. Anal. 20, 233–256.
Stephenson, H.G. (Ed.), 2019. The Platreef Magma Event at the World-Class Turfspruit Ni-cu-PGE Deposit: Implications for Mineralisation Processes and the Bushveld Complex Stratigraphy. Cardiff University. Unpublished PhD thesis,. 532pp.
Teigler, B., Eales, H.V., 1996. The Lower and Critical Zones of the western limb of the Bushveld Complex as intersected by the Nooitgedacht boreholes. In: Geological Survey of South Africa Bulletin, 111. Geoscience, Council for, 126pp.

Van De Kamp, P.C., Leake, B.E., Senior, A., 1976. The petrography and geochemistry of some Californian arkoses with application to identifying gneisses of metasedimentary origin. J. Geol. 84, 195–212.
van der Merwe, M.J., 1978. The Geology of the Basic and Ultramafic Rocks of the Potgietersrus Limb of the Bushveld Complex. Unpublished PhD thesis,. University of the Witwatersrand, 176 p.
Vantongeren, J.A., Mathez, E.A., Kelemen, P.B., 2010. A felsic end to Bushveld differentiation. J. Petrol. 51, 1891–1912.
White, J.A., 1994. The Potgietersrus Prospect - Geology and exploration history: XVth CMMI Congress, 3. SAIMM, Johannesburg, pp. 173–181.
Wilson, A.H., 2015. The earliest stages of emplacement of the eastern Bushveld Complex: development of the Lower Zone, Marginal Zone and Basal Ultramafic Sequence. J. Petrol. 56, 347–388.
Wilson, A., Chunnett, G., 2006. Trace element and platinum group element distributions and the genesis of the Merensky Reef, Western Bushveld Complex, South Africa. J. Petrol. 47, 2369–2403.
Xiao, B., Chen, H., Hollings, P., Wang, Y., Yang, J., Wang, F., 2018. Element transport and enrichment during propylitic alteration in Paleozoic porphyry Cu mineralization systems: insights from chlorite chemistry. Ore Geol. Rev. 102, 437–448.
Yuan, Q., Namur, O., Fischer, L.A., Roberts, R.J., Lü, X., Charlier, B., 2017. Pulses of plagioclase-laden magmas and stratigraphic evolution in the Upper Zone of the Bushveld Complex, South Africa. J. Petrol. 58, 1619–1643.
Yudovskaya, M.A., Kinnaird, J.A., Sobolev, A., Kuzmin, D.V., McDonald, I., Wilson, A.H., 2013. Petrogenesis of the Lower Zone olivine-rich cumulates beneath the Platreef and their correlation with recognized Occurrences in the Bushveld Complex. Econ. Geol. 108, 1923–1952.
Yudovskaya, M.A., Kinnaird, J.A., Grobler, D.F., Costin, G., Abramova, V.D., Dunnett, T., Barnes, S.J., 2017. Zonation of Merensky-style platinum-group element mineralization in Turfspruit thick reef facies (northern limb of the Bushveld Complex). Econ. Geol. 112, 1333–1365.
Zheng, Y.C., Gu, L., Tang, X., Wu, C., Li, C., Liu, S., 2013. Geology and geochemistry of highly metamorphosed footwall alteration zones in the Hongtoushan volcancogenic massive sulfide deposit, Liaoning Province, China. Resour. Geol. 61, 113–139.
Zheng, R., Li, J., Zhang, J., Xiao, W., 2021. A prolonged subduction-accretion in the southern Central Asian Orogenic Belt: insights from anatomy and tectonic affinity for the Beishan complex. Gondwana Res. 95, 88–112.